J. Fluid Mech. (2009), *vol.* 625, *pp.* 205–248.
doi:10.1017/S0022112008005557 Printed in the United Kingdom

Transition to turbulence in the wake of a fixed sphere in mixed convection

MIROSLAV KOTOUČ, GILLES BOUCHET AND JAN DUŠEK†

Institut de Mécanique des Fluides et des Solides, Université de Strasbourg, France

(Received 3 July 2008 and in revised form 10 December 2008)

The thermal effect on axisymmetry breaking and transition to turbulence in the wake of a fixed heated sphere is investigated in the mixed convection configurations commonly known as 'assisting'and 'opposing' flows in which the buoyancy tends, respectively, to accelerate and decelerate the flow. The study is carried out in the Ri–Re parameter plane (Ri being the mixed convection parameter – the Richardson number) for two values of Prandtl number – 0.72 (≈air and many gases) and 7 (≈water). We show that convection affects considerably the transition (as compared to that observed in the wake of an unheated sphere) even at moderate Richardson numbers. The latter are taken to be positive in assisting flow and negative in opposing one. In this notation, it can be said that convection shifts the primary-instability threshold to higher Reynolds numbers with increasing Richardson number. In assisting flow, the primary bifurcation is always regular, but at $Ri \geqslant 0.6$ it appears in azimuthal subspaces associated with higher azimuthal wavenumbers $m > 1$. The transition scenario is characterized by a large variety of regimes explainable by nonlinear interactions between different azimuthal subspaces. On the side of higher (positive) Richardson numbers the axisymmetric flow is found stable up to $Re = 1400$ at $Pr = 0.72$ and $Ri = 0.7$. In opposing flow, the $m = 1$ subspace is always the most unstable, but the regular bifurcation gives way to a Hopf one at $Ri < -0.1$. Close to the junction of both bifurcations a similar variety of regimes precedes the transition to chaos as in assisting flow. On the side of negative Richardson numbers the primary (Hopf) bifurcation threshold is found as low as $Re = 100$ at $Ri = -0.25$ and at both investigated Prandtl numbers. After a primary periodic regime characterized by vortex shedding with a symmetry plane, the transition proceeds via a series of increasingly irregular helical regimes.

1. Introduction

The mixed convection past solid bodies has many practical applications in cooling, heating, sedimentation (Gan *et al.* 2003), melting (McLeod, Riley & Sparks 1996), combustion (Ayyaswamy 1999), vaporization (Chiang & Sirignano 1993) and many other fields of engineering and chemistry. Special interest has been focused on heated infinite cylinders and spheres as prototypical solid bodies. The case of the sphere presents the advantage of avoiding the end effects of the cylinder and of having direct application in sedimentation and melting. A fixed heated sphere represents a prototypical heat source and provides a configuration for which experiments and

† Email address for correspondence: dusek@imfs.u-strasbg.fr

numerical simulations can be brought closer than for any other situation. Not only heat transfer but also the modification of hydrodynamic forces by convection effects are of interest. A hot sedimenting particle is submitted to hydrodynamic forces due to its falling velocity and the flow of the heated fluid induced by buoyancy effects. It is clearly seen that the forces are the result of a mixed forced and convective flow, which is commonly known as mixed convection. In the case of a hot falling sphere the convection adds up to the forced flow and accelerates the fluid in the wake with respect to the particle. The flow is then called 'assisting'. In the opposite case, that of a cold falling sphere or a hot ascending one, the buoyancy decelerates the wake. Such a flow is called 'opposing'. 'Cross-flow' with a flow direction perpendicular to gravity has mostly been investigated for cylinders (Lecordier, Hamma & Paranthoen 1991; Wang, Trávníček & Chia 2000; Wu & Wang 2007), although a certain number of, basically experimental, results are also available for spheres (e.g. Yuge 1960). The investigation of cross-flows aims mainly at cooling.

Experimental investigations concern mostly both the assisting and opposing flows past a sphere. The work by Yuge (1960), Klyachko (1963), Katoshevski *et al.* (2001), Bar-Ziv *et al.* (2002), Mograbi *et al.* (2002) and Mograbi & Bar-Ziv (2005*a*, *b*) focused mainly on acquisition of data concerning the drag and heat flux (drag coefficient and Nusselt number). Work investigating details of the flow is less common (see Tang & Johnson 1990). Experimental investigations of heated spheres present numerous technical problems, which stimulated, very early, numerical simulations. Most of the bibliography is involved with pure convection (see Geoola & Cornish 1982; Dudek *et al.* 1988; Jia & Gogos 1996). Numerical papers dealing with mixed convection past a sphere are less frequent. The earliest works used approximations to bring the problem within reach of available computing power. Hieber & Gebhart (1969) considered small Reynolds and Grashof numbers and applied asymptotic expansions to obtain approximations for the drag coefficient and Nusselt number. Chen & Mucoglu (1977) and Mucoglu & Chen (1978) solved the flow past a heated sphere with a boundary layer approximation assuming high Reynolds (Re) and Grashof (Gr) numbers. Such a problem presents only one parameter (the Richardson number, $Ri = Gr/Re^2$, for a fixed Prandtl number, considered equal to 0.7). Both extreme cases of large and small Richardson numbers are investigated for the relevance of the mixed convection and inertia effect. Probably the first to solve the full Navier–Stokes–heat transfer problem, albeit limited to the case of assisting flow, were Wong, Lee & Chen (1986) for Reynolds numbers ranging from 5 to 100 and for several values of Richardson number. A recent simulation of assisting flow by Bhattacharyya & Singh (2008) focuses on $Re = 1, 150$ and 200 and $Ri = 0, 0.5$ and 1 and states the recirculation zone disappears due to the convective plume. Nguyen, Paik & Chung (1993) solved the conjugate problem including the heat conduction inside the sphere for Reynolds numbers ranging from 10 to 100 and Grashof numbers up to 10^5 (Richardson numbers up to 40). They found the effect of gravity-induced flow on the drag coefficient and Nusselt number to be small. Mograbi & Bar-Ziv (2005*a*) found a very significant gravity-induced effect at Reynolds numbers and Grashof numbers smaller than 1. In particular, in the case of opposing flow, they discovered the formation of a large recirculation 'when buoyant forces overcome inertia and viscous forces'. This situation is found to occur at $\zeta \approx 1$ (where ζ is a mixed convection parameter introduced by Mograbi & Bar-Ziv 2005*a* and defined as $\zeta = 1/Ri$). For $\zeta < 1$ the sphere is immersed in a recirculation plume, and the drag is found to be practically constant and equal to the value due to pure convection. For $\zeta \gg 1$ the proportionality to the square of velocity (square of the Reynolds number) characteristic of drag without buoyant

effects is recovered. The recirculation seems to grow to infinity: 'in order to obtain adequate results for the mixed convection problem the computational domain must be enormous'. At $Gr = 0.01$ and $\zeta = 0.81$, the radius of the recirculation is found to exceed 250 sphere diameters.

The published numerical simulations of mixed convection past a sphere map only very sparsely the space of all three parameters (Reynolds, Richardson and Prandtl numbers), and are all axisymmetric. For this reason, in a recent paper (see Kotouč, Bouchet & Dušek 2008), we investigated axisymmetric assisting flow in a large domain of the three-parameter space. The stabilizing effect of convection in assisting flow let us expect that axisymmetric simulations might remain valid up to much higher Reynolds numbers than in the wake of an unheated sphere we explored albeit imperfectly as appears in the present paper – the question of validity of axisymmetric simulations. In aerosols, the particles are usually so small that the flow regimes do not exceed $Re, Gr \sim 1$, but as soon as the asymptotic velocity or the convection becomes large the flow has to be expected to leave the axisymmetric laminar regime. In view of increasingly frequent and increasingly accurate numerical results appearing in literature, setting accurate limits of the stability of axisymmetric flow has become important. As a consequence we completed the axisymmetric investigation of assisting flow in Kotouč *et al.* (2008) by computing the threshold of the primary, axisymmetry-breaking bifurcation up to a Richardson number of 0.7 at $Pr = 0.72$ and up to $Ri = 0.35$ for $Pr = 7$. The threshold was obtained by evaluating the least stable eigenvalue of the linearized Navier–Stokes operator projected onto the $m = 1$ azimuthal subspace known to be the least stable in all similar configurations such as an unheated sphere wake (Natarajan & Acrivos 1993; Johnson & Patel 1999; Ormières & Provansal 1999; Ghidersa & Dušek 2000) and a round cold jet (Michalke 1984).

One of the results of Kotouč *et al.* (2008) consists in presenting a state diagram delimiting axisymmetric flow regimes arising due the onset of a convective plume in the recirculation zone (reported also in Bhattacharyya & Singh 2008). The diagram, as well as the whole previous study, was delimited by the primary-bifurcation threshold. The present paper aims at investigating what happens between the primary bifurcation and the onset of a chaotic wake considered to represent an early stage of turbulence. In § 2, we briefly review and discuss the mathematical formulation of the problem and the used numerical method. In §§ 3 and 4 the breaking of axisymmetry is studied. Section 5 sums up the method of presentation of the transition states found in following sections. Section 6 is devoted to the determination of limits of the scenario known to apply to the wake of an unheated sphere. The transitional regimes specific for assisting and opposing flows are investigated in §§ 7 and 8, respectively. The results are summed up in the form of state diagrams in figures 2 and 4. Section 9 focuses on hydrodynamic forces and the heat transfer. For more graphic material refer to Kotouč (2008).

2. Mathematical formulation and numerical method

Our numerical simulations represent a heated sphere with a constant surface temperature immersed in a cold incompressible fluid. For the problem description and coordinate system definition, see figure 1(*a*). This situation is mathematically described by a system of Navier–Stokes equations coupled with energy equation (see e.g. Jia & Gogos 1996) for the unsteady flow of an incompressible fluid with constant properties. The buoyancy effects are characterized, in agreement with all the numerical work cited above, by the Boussinesq approximation. The Boussinesq approximation,

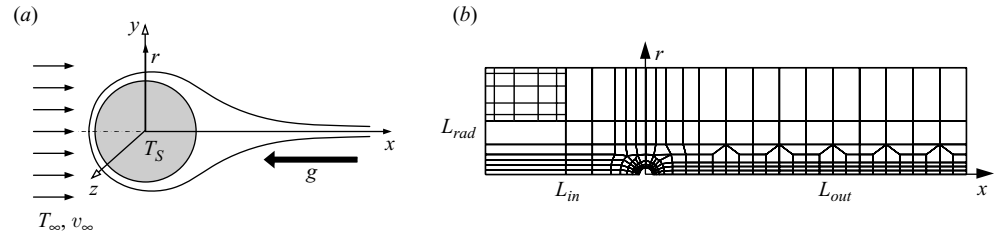

FIGURE 1. (*a*) Problem description and coordinate system; (*b*) example of a computational domain of 230 elements with collocation points of the upper left element (the order of Gauss–Lobatto–Legendre polynomials being six in both directions).

discussed briefly in Kotouč *et al.* (2008), limits the scope of applications but has the advantage of setting a mathematical framework that has become standard and allows to reduce the parameter space to three widely used non-dimensionalized parameters.

In Kotouč *et al.* (2008) an example of configuration satisfying the limitations of the Boussinesq approximation is suggested: a sphere of 11 cm diameter, placed in an airflow of $0.2\,\mathrm{m\,s^{-1}}$ and heated 8° above the surrounding temperature represents a configuration with $Re = 1500$ and $Ri = 0.7$. In these conditions the viscous dissipation term is of the order of 10^{-6} and is not considered in agreement with all the numerical bibliography using the Boussinesq approximation. In practical applications, the weakest point of the so defined model is the Boussinesq approximation itself, namely the constant fluid properties, not the absence of viscous dissipation. It is widely admitted that, in air, the tolerable temperature difference is at most about 15 K at 20° C and, in water, as few as 2 K at the same temperature.

The fluid properties are the density ρ at the temperature far from the sphere, the kinematic viscosity ν, the thermal conductivity λ, the specific heat at constant pressure c_p and the coefficient of thermal expansion β. The equations are non-dimensionalized using the following scalings: the sphere diameter d as a length scale, the free stream velocity v_∞ as a velocity scale, d/v_∞ as a time scale and ρv_∞^2 as a pressure scale. The dimensionless temperature is defined as $T^* = (T - T_\infty)/(T_S - T_\infty)$ with T_∞ the fluid temperature far from the sphere and T_S the temperature of the sphere surface (assumed to be constant and uniform) . In what follows, we omit the symbol '*' in the notation of the non-dimensionalized quantities; thus $\boldsymbol{v}$, p and T stand for non-dimensionalized velocity, pressure and temperature, respectively. In plots representing quantities vs. time in this paper, the non-dimensionalized time is taken in time units equal to d/v_∞. The dimensionless equations become

$$\nabla \cdot \boldsymbol{v} = 0, \tag{2.1}$$

$$\frac{\partial \boldsymbol{v}}{\partial t} + (\boldsymbol{v} \cdot \nabla)\boldsymbol{v} = -\nabla p + \frac{1}{Re}\nabla^2 \boldsymbol{v} + Ri\, T\, \boldsymbol{i}, \tag{2.2}$$

$$\frac{\partial T}{\partial t} + (\boldsymbol{v} \cdot \nabla)T = \frac{1}{Re.Pr}\nabla^2 T, \tag{2.3}$$

where $\boldsymbol{i} = \boldsymbol{v}_\infty / v_\infty$ stands for the unit vector of dimensionless far stream velocity. The non-dimensionalization reduces the parameters to three non-dimensional numbers – Reynolds number (Re), Richardson number (Ri) and Prandtl number (Pr) – defined as follows:

$$Re = \frac{v_\infty d}{\nu}, \quad Ri = -\frac{\beta\,(\boldsymbol{i} \cdot \boldsymbol{g})\,(T_S - T_\infty) d}{v_\infty^2}, \quad Pr = \frac{\nu}{\kappa}, \tag{2.4}$$

where κ stands for the thermal diffusivity; $\kappa = \lambda/\rho c_p$; and $\boldsymbol{g}$ is the gravitational acceleration.

The notation accommodates both the assisting and opposing flows represented, respectively, by a positive and a negative sign of the Richardson number, Ri. Experimentally, the assisting (opposing) flow is obtained e.g. by placing a heated sphere into an upward (downward) oriented vertical flow, which yields indeed a positive (negative) sign in the definition of the Richardson number of (2.4).

The sphere is placed in a cylindrical domain with its axis parallel to the flow direction. The method of spatial discretization is that of earlier papers (see Ghidersa & Dušek 2000; Jenny & Dušek 2004; Kotouč *et al.* 2008), combining a spectral element discretization in the radial–axial plane with a spectral azimuthal decomposition (expansion into azimuthal Fourier modes, numbered by integer $m \geqslant 0$ in what follows). Figure 1 presents an example of a spectral element mesh in the radial–axial plane. The method proved to be optimal for the investigation of flows undergoing axisymmetry breaking for two basic reasons. Firstly it allows for an easy theoretical analysis using the linear and weakly nonlinear theories, and secondly it provides an optimal numerical efficiency making it possible to simulate relatively complicated dynamics of three-dimensional flows at low costs. The reduced costs are especially welcome if parametric studies are tackled. In Jenny, Dušek & Bouchet (2004) a two-parametric study could be obtained in this way in the configuration of a freely moving sphere. The minimal description of the configuration of the heated fixed sphere comprises three parameters, and in what follows, we investigate four parameter half-planes in this space. The complexity of the scenario in each half-plane appears to be much higher in presence of thermal effects, and the necessity to push the investigation to Reynolds numbers exceeding 1000 requires a very high resolution of the boundary layer. A sufficient spatial resolution appeared to be especially crucial in removing spurious instabilities and spurious regimes excited numerically by the spectral element discretization, namely inaccuracies at the spectral element interfaces (see Patera 1984).

The quest for the highest possible accuracy at the lowest costs led us to extensive testing and optimization of the numerical parameters. The size of the domain, as well as the order of polynomials in each spectral element, was thoroughly tested for both Prandtl numbers in all the simulated regimes and adapted so that neither its extension upstream, downstream and sidewise nor an increase of the number of collocation points in each element brought significant changes to the flow. Not only the computed drag coefficient and Nusselt number but, in the transitional domain, also the primary-instability threshold and the stability of all investigated strongly nonlinear regimes were verified to be insensitive to further mesh refinement and also to the increase of the number of used azimuthal modes (see Kotouč *et al.* 2008 for more details on the testing). Each regime having its specificity (e.g. a higher Prandtl number implies a thinner thermal boundary layer necessitating a higher resolution; low Reynolds numbers and high negative Richardson number require large lateral and upstream domain extension), a great variety of spectral element meshes had to be used to get an optimal discretization. Table 1 sums up the discretization parameters of the domains: the domain size, the order of used Gauss–Lobatto–Legendre polynomials in both directions in each element and the overall number of elements in the mesh as a function of Reynolds and Prandtl numbers. For $Pr = 7$, where the boundary layers are much thinner than for $Pr = 0.72$, the mesh was significantly refined in the boundary layer of the sphere, which makes the overall number of elements for $Pr = 7$ always higher than for $Pr = 0.72$. The thin thermal boundary layer obliged us also to restrict the scope of investigated Reynolds numbers from up to $Re \leqslant 1500$ at

Assisting flow ($Ri > 0$)

$Pr = 0.72$						$Pr = 7$					
Re	$\frac{L_{in}}{d}$	$\frac{L_{out}}{d}$	$\frac{L_{rad}}{d}$	NE	NP	Re	$\frac{L_{in}}{d}$	$\frac{L_{out}}{d}$	$\frac{L_{rad}}{d}$	NE	NP
50–99	50	60	52	230	6	50–99	50	60	52	312	7
100–199	25	60	25	212	7	100–199	25	60	25	270	8
200–399	12	25	8	169	8	200–399	12	24	8	295	8
400–999	12	25	8	169	10	400–600	12	24	8	295	10
1000–1400	12	24	8	230	12						

Opposing flow ($Ri < 0$)

$Pr = 0.72$						$Pr = 7$					
Re	$\frac{L_{in}}{d}$	$\frac{L_{out}}{d}$	$\frac{L_{rad}}{d}$	NE	NP	Re	$\frac{L_{in}}{d}$	$\frac{L_{out}}{d}$	$\frac{L_{rad}}{d}$	NE	NP
50–99	25	64	25	270	6	50–99	25	64	25	270	7
100–199	12	25	8	169	7	100–199	12	25	8	169	8
200–350	12	25	8	169	8	200–350	12	24	8	295	8

TABLE 1. Upstream (L_{in}/d) and downstream (L_{out}/d) lengths and radii (L_{rad}/d) of the computational domain; overall number of elements in the mesh (NE) and number of collocation points per element direction (NP) for intervals of Re indicated in the first column.

$Pr = 0.72$ to $Re \leqslant 600$ at $Pr = 7$. Finally the number of used modes in the Fourier azimuthal expansion was also tested and varied in three-dimensional simulations. The highest mode used varied from 3 to 10, depending on the distance from the threshold of axisymmetry breaking.

3. Axisymmetric assisting flow and primary, axisymmetry-breaking bifurcations

3.1. *Axisymmetric flow*

For assisting flow, the axisymmetric flow regime was investigated in Kotouč *et al.* (2008). The most striking feature of assisting flow is the onset of a convective plume in the recirculation zone downstream of the sphere. Three different regimes could be distinguished: a completely attached flow such as that widely known to be typical for a flow past an unheated sphere at Reynolds numbers smaller than 20 (see Bouchet, Mebarek & Dušek for a more detailed discussion). At $Pr = 0.72$, the convection shifts the existence of attached flow up to $Re = 700$ at $Ri = 0.7$. At Richardson numbers smaller than 0.4 the boundary layer detaches to form a recirculation zone along the flow axis. At $Ri \geqslant 0.4$ the convection is, however, strong enough to let a convective plume pierce the recirculation zone and to make the boundary layer reattach upstream of the rear stagnation point. Instead of a usual recirculation zone we are in presence of a recirculation torus. At the very onset of this flow regime (when Re is increased and Ri kept fixed) the torus is very thin. It grows with growing Reynolds number until it reaches the flow axis and forms a usual recirculation zone. The same behaviour was observed at $Pr = 7$ albeit shifted to lower Richardson numbers. In view of the experience with axisymmetry breaking an attempt was made to set the upper limit of stability of the axisymmetric flow. The results were summed up in two diagrams, in the two selected $Pr =$ constant planes with a horizontal Ri axis and a vertical Re axis

delimited from above by the maximum Reynolds number at which both the dynamic and the thermal boundary layers could be resolved at acceptable costs and at the right (on the side of higher Richardson numbers) by the Richardson number at which the axisymmetric flow computed at the highest Reynolds number was still found to become unstable. The purpose of the present section is to fill the unmapped domain above the instability threshold of Kotouč *et al.* (2008). The new diagrams presented in figure 2 include the axisymmetric regimes described in Kotouč *et al.* (2008) below the thick lines marking the primary-instability threshold.

3.2. *Primary bifurcation and loss of axisymmetry*

As explained in Ghidersa & Dušek (2000), the linear analysis of the breaking of axisymmetry can be decomposed into a sequence of independent eigenvalue problems, each being resolved in a subspace associated with a given azimuthal wavenumber of perturbations. The primary instability arises in the subspace in which the first eigenvalue becomes unstable (i.e. the real part of which becomes positive). It is well known that in the wake of an unheated sphere this subspace corresponds to $m = 1$ and that the unstable eigenvalue is real. (The primary bifurcation is regular.)

In Kotouč *et al.* (2008), the investigation of the threshold of axisymmetry breaking of the flow was limited to a subspace corresponding to the azimuthal subspace with wavenumber $m = 1$. More recent numerical investigations have shown, however, that at $Pr = 0.72$, the first mode to become unstable corresponds to the wavenumber $m = 1$ only for $Ri < 0.590$. For $0.590 < Ri < 0.714$, the primary instability sets in the $m = 2$ subspace and for $0.714 < Ri \leqslant 0.75$ (where $Ri = 0.75$ is the upper limit of the investigation) in the $m = 3$ subspace. The three cases are distinguished by three decreasing levels of grey in which the line representing the primary-bifurcation threshold is plotted in figure 2. More accurately, the point at which both (real) eigenvalues become unstable in $m = 1$ and $m = 2$ subspaces was found to be $Ri = 0.590$ and $Re = 991$, and the same point at which $m = 2$ and $m = 3$ subspaces become simultaneously unstable corresponds to $Ri = 0.714$ and $Re = 1309$. Although the investigation was not pushed beyond it is likely that the azimuthal wavenumber of the most unstable mode grows very rapidly further with Ri. The common feature of all cases is that the axisymmetry is broken via a regular bifurcation.

The reason of the increase of the azimuthal wavenumber of the primary instability is the changing aspect of the base flow with increasing Ri described above in § 3.1. As already said, a convective plume limits the recirculation to a recirculation torus off the flow axis starting from $Ri = 0.4$ at $Pr = 0.72$. In an interval of Richardson numbers smaller than 0.6 this torus grows with Re and eventually reaches the flow axis before the instability sets in. Beyond $Ri = 0.6$, the axisymmetry-breaking instability sets in at a stage at which the torus has not yet reached the flow axis. The unstable base flow presents thus a recirculation zone with a cross-section of a significantly smaller length than its radius. As a result, the base flow is more receptive to perturbations with a higher azimuthal wavenumber. Figure 3 shows three axisymmetric flow patterns slightly above the three-dimensionality threshold. The flow in figure 3(a) becomes unstable in the $m = 1$ subspace – the recirculation zone touches the flow axis, and the size of the cross-section is comparable to its radius. Figure 3(b) presents a flow in which the most unstable mode is associated with the wavenumber $m = 2$ – the recirculation torus no longer touches the flow axis. Finally, figure 3(c) presents a thin recirculation torus in base flow becoming unstable in the $m = 3$ subspace.

Within the limits of the investigated parameter plane at $Pr = 7$, given by the CPU limitations, the threshold of axisymmetry breaking was always found at regimes

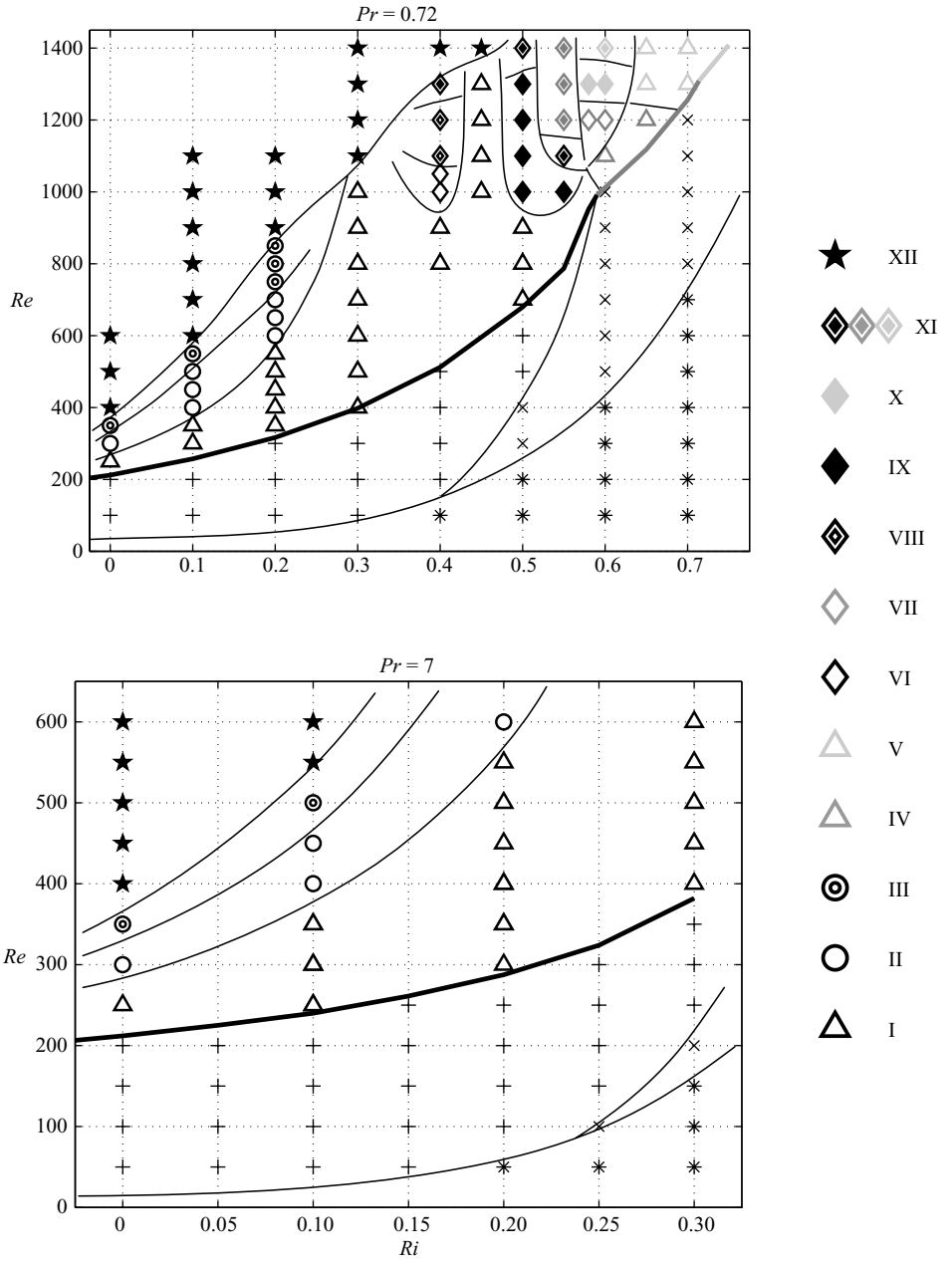

FIGURE 2. Assisting flow: diagrams of regimes. Thick line: primary-instability threshold. Shading: most unstable subspace – black: $m = 1$; grey: $m = 2$; light grey: $m = 3$. Below the threshold: axisymmetric regimes. ($*$ attached flow, $+$ recirculation at the flow axis, $\times$ recirculation off the flow axis). Three-dimensional states – triangles: steady (I, IV, V); empty circles (II): periodic vortex shedding with symmetry plane; empty diamonds (VI, VII): periodic with symmetry plane without vortex shedding; full diamonds (IX, X): periodic rotating; double symbols (III, VIII, XI): quasi-periodic states; $\star$ (XII): chaos.

in which the recirculation torus reached the axis. As a consequence, the primary instability was always found to set in with an amplified mode lying in the $m = 1$ subspace. Let us note that the CPU time needed to investigate regimes in the upper

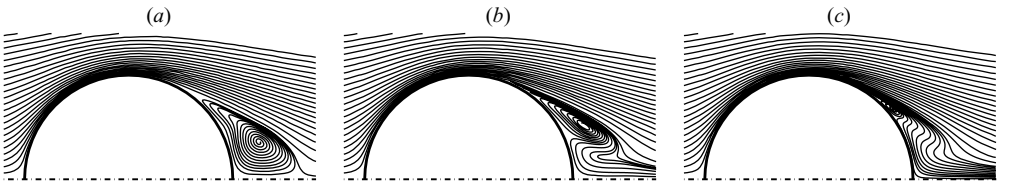

FIGURE 3. Streamlines of three different axisymmetric flow patterns, presenting (*a*) a recirculation zone at the flow axis at $Ri = 0.55$, $Re = 800$, (*b*) a recirculation torus off the flow axis at $Ri = 0.6$, $Re = 1020$ and (*c*) a confined recirculation torus off the flow axis at $Ri = 0.75$, $Re = 1420$.

$Pr = 0.72$

Ri	0	0.1	0.2	0.3	0.4	0.5	0.55	0.590	0.6	0.65	0.7	0.714	0.75
Re_1	212.0	257.1	316.4	397.7	512.0	679.4	786.9	991.4	1012	1118	1271	1309	1409
m	1	1	1	1	1	1	1	1, 2	2	2	2	2, 3	3

$Pr = 7$

Ri	0	0.05	0.1	0.15	0.2	0.25	0.3
Re_1	212.0	225.1	240.0	261.3	287.5	324.1	382.3
m	1	1	1	1	1	1	1

TABLE 2. Thresholds of the primary (regular) bifurcation Re_1 and corresponding most unstable azimuthal mode m depending on the Richardson number for both $Pr = 0.72$ and $Pr = 7$. Two values for most unstable azimuthal mode for one Richardson number mean that both modes become unstable at the same time (border cases).

right part of the diagram is not proportional to the CPU time needed to cover one time unit with a refined spatial discretization. By far the greatest part of the increase is due to the necessity to run the simulation for many time units to converge to an asymptotic regime not speaking about the CPU consumed for mesh optimization and for removing spurious regimes. Just to provide an example, the steady regime at $Ri = 0.3$ and $Re = 600$ (upper right corner) of the $Pr = 7$ diagram in figure 2 could be identified as indeed asymptotically steady only after many weeks of simulations. It can be conjectured that the primary instability will appear in $m > 1$ subspaces at Richardson numbers lying beyond the scope of the diagram.

The thick solid, black, grey and light grey lines connect the thresholds of the onset of three-dimensionality with the most unstable mode corresponding to the azimuthal wavenumbers $m = 1$, $m = 2$ and $m = 3$. The computed instability thresholds for both investigated Prandtl number values are recalled in table 2. The three-dimensional regimes represented above the threshold line are analysed in the following sections.

4. Axisymmetric opposing flow and loss of its axisymmetry

4.1. *Axisymmetric flow*

In contrast to the stabilizing effect of the buoyancy-driven flow in the assisting flow configuration, resulting in a later appearance of the axisymmetric recirculation zone downstream of the sphere for higher Richardson numbers (see Kotouč *et al.* 2008), the effect of buoyancy in opposing flow is opposite – it lowers the critical Reynolds number Re_{rec} of the onset of the recirculation zone. The critical Reynolds number

$Pr = 0.72$

Ri	0	−0.1	−0.119	−0.133	−0.153	−0.172	−0.2	−0.3	−0.4	−0.5
Re_1	212	180	175	171.6	160	150	127.2	75.7	46.3	29.4
St	0	0	0	0, 8.42×10^{-2}	7.99×10^{-2}	7.61×10^{-2}	7.28×10^{-2}	5.16×10^{-2}	2.48×10^{-2}	1.54×10^{-2}

$Pr = 7$

Ri	0	−0.05	−0.098	−0.1	−0.13	−0.15	−0.156	−0.2	−0.3	−0.4
Re_1	212	201	185	183.6	173.6	167.8	166.3	144.2	92	61.6
St	0	0	0	4.33×10^{-3}	5.03×10^{-3}	5.57×10^{-3}	5.92×10^{-3}, 8.79×10^{-2}	8.58×10^{-2}	8.12×10^{-2}	7.64×10^{-2}

TABLE 3. Thresholds of the primary instability and the respective Strouhal numbers (imaginary parts of the unstable eigenvalues divided by 2π).

for the onset of recirculation decreases when the absolute value of Ri increases in opposing flow. Although we did not perform a detailed study of the dependence of Re_{rec} on the Richardson number (the reason being the necessity of using completely different – extremely large but looser – computational domains at very low Reynolds numbers), we found that at $Pr = 0.72$ and $Ri = -0.3$, -0.6 and -0.9, the recirculation zone exists already, respectively, at $Re = 10$, 5 and 1. Moreover, we found that at these very low Reynolds numbers and relatively large Richardson numbers, a further increase of the absolute value of Ri at a constant Re makes the flow become unstable. The buoyancy reverses the flow direction close to the sphere and yields a reverse plume. Actually, such a flow becomes three-dimensional and immediately chaotic; thus there is not much interest in pushing the investigation of axisymmetric flow to this domain of parameters. Nevertheless, the reversal of the thermal plume was observed at $Ri \approx -0.8$ at $Re = 10$ and at $Ri \approx -1.5$ at $Re = 1$. The study of the transition to three-dimensionality of the thermal plume at high Ri in opposing flow is beyond the scope of this paper.

The flow at $Pr = 7$ presents, at all parameter sets, a smaller recirculation zone. This agrees with the observation that the size of a recirculation zone is linked to the transition to three-dimensionality – the transition at $Pr = 0.72$ sets in at a lower Re at a constant Ri or at a lower Ri at a constant Re than at $Pr = 7$.

It is also worth noting that there is no qualitative change in the flow aspect of the base flow at $Ri \approx -0.13$ when the primary bifurcation changes from regular to Hopf.

4.2. *Primary bifurcation and loss of axisymmetry*

At $Pr = 0.72$ the primary instability was found in the $m = 1$ azimuthal subspace only within a limited interval of Richardson numbers. It was argued that it could be explained by the presence of a convective plume limiting the recirculation to a recirculation torus getting thinner and thinner. In opposing flow, the trend is rather towards an enhanced recirculation. The recirculation zone develops at flow axis at decreasing Reynolds numbers so that the instability sets in systematically in a base flow with a well-developed recirculation. The primary instability has thus to be expected to arise always in the $m = 1$ subspace. Moreover, in agreement with the general observation of the link between the size of the recirculation domain and the instability of the base flow, the convection is to be expected to have a destabilizing effect. The most striking feature of the opposing flow results from a different variation of the real parts of the least stable real eigenvalue and those of the least stable eigenpair. Table 3 sums up the thresholds of the primary instability depending on the Richardson number.

At $Pr = 0.72$, table 3 shows that at $Ri = -0.13$ the complex eigenpair starts to be more unstable than the real eigenvalue, i.e. at $Ri = -0.133$ and $Re = 171.6$, the regular bifurcation gives way to a Hopf one. This is to be expected to have a significant impact on the next stages of transition in the same way, as will be shown in the case of assisting flow, that the interplay of unstable azimuthal subspaces is responsible for the specificities of the scenario. The results dealing with opposing flow are summarized, again, in the form of two state diagrams in the $Pr = 0.72$ and $Pr = 7$ planes parametrized by varying Richardson and Reynolds numbers plotted in figure 4. In principle, both diagrams for $Ri > 0$ and $Ri < 0$ at the same Pr can be joined along the $Ri = 0$ line. Because of the different scales of plots we found it preferable to keep the figures separate. The primary-instability threshold is materialized by a thick line for the regular bifurcation and a thick dotted line for the Hopf one.

At $Pr = 7$ we found a still more interesting situation. If the Reynolds number is progressively increased from some subcritical value at a fixed Richardson number between -0.098 and -0.156 a pair of complex conjugate eigenvalues crosses the imaginary axis yielding a Hopf bifurcation, but very soon after it collides and forms a pair of two real eigenvalues. As a result, this Hopf bifurcation, characterized by a very small Strouhal number, is related to the same eigenvalue as the regular one, but the real eigenvalue has become complex in a collision with a second, more stable, real eigenvalue. Figure 5 represents the details of this eigenvalue collision at a constant $Ri = -0.1$ and for $Re \in [180, 190]$ obtained by linear analysis. At $Re = 180$ we are in presence of a stable complex eigenpair. (The point $Ri = -0.1$, $Re = 180$ lies below the primary-instability threshold in figure 4.) The threshold lies at $Re = 183.5$; i.e. the eigenpair crosses the imaginary axis between $Re = 180$ and $Re = 185$. The primary-instability threshold corresponds to a Hopf bifurcation. At $Re = 189$ both complex eigenvalues collide in the $Re(\lambda) > 0$ half-plane. They give rise to a pair of real, initially unstable, eigenvalues, one of which moves to the left and the other to the right. At $Re = 190$ the left eigenvalue has already become stable. The complex eigenpair has, of course, a zero imaginary part at the collision point. The imaginary part of the complex eigenvalue at the instability threshold is about 0.0027 (at this Richardson number), which corresponds to the Strouhal number $St = 4.10^{-4}$; i.e. the characteristic frequency of this Hopf bifurcation is much smaller than that of the complex eigenpair responsible for the primary Hopf bifurcation found at $Pr = 0.72$.

Viewed along the primary-bifurcation threshold line followed from zero to higher (more negative) Richardson numbers, for $Ri > -0.1$ the least stable eigenvalue is real and is accompanied by a second more stable eigenvalue. At $Ri = -0.1$ both real eigenvalues meet at the primary-instability threshold and give rise to a complex eigenpair, which represents the least stable eigenvalues for $Ri < -0.1$. The low-frequency Hopf bifurcation is a continuation of the regular one and represents the primary bifurcation in the interval of Ri varying from -0.098 to -0.156. It is interesting to note that the middle of this interval lies at $Ri = -0.13$, the value at which the regular and Hopf bifurcations meet at $Pr = 0.72$. Starting from Richardson number $Ri = -0.156$ the 'ordinary' high-frequency Hopf bifurcation with $St \sim 0.1$ sets in because the high-frequency eigenpair becomes more unstable. The newly appeared low-frequency eigenpair is directly visible on the transition scenario only in the closest vicinity of the primary-bifurcation threshold; nevertheless it complicates the scenario far into the transition.

In the same way as for assisting flow, the primary-instability threshold only weakly depends on the Prandtl number. This is approximately true also for the thresholds of higher supercritical regimes.

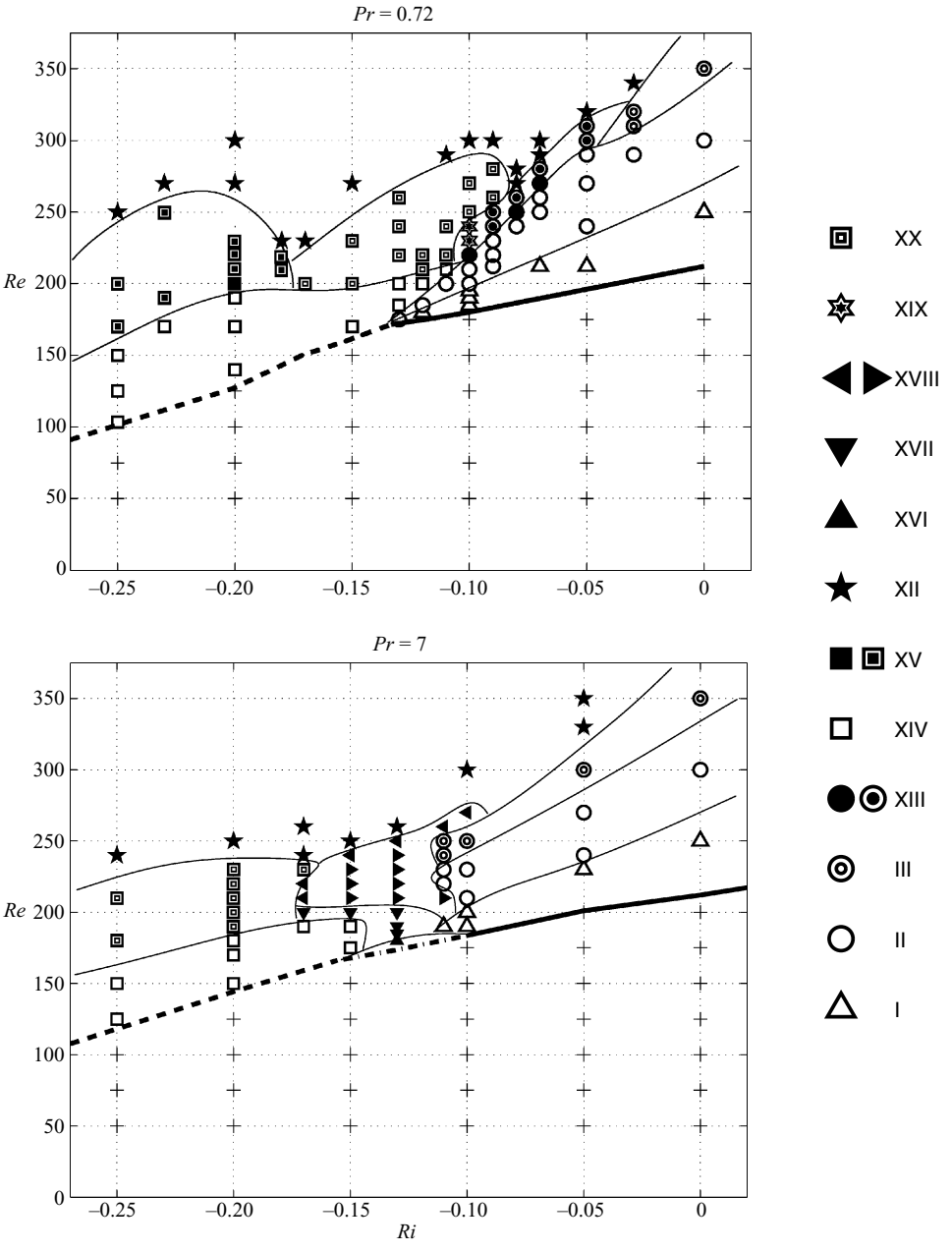

FIGURE 4. Diagrams of regimes of opposing flow. Thick line: regular bifurcation; dashed line: high-frequency Hopf bifurcation; dash-dotted line ($Pr = 7$): low-frequency Hopf bifurcation. XIII: slowly rotating helical regime with a non-zero regular mode – perfectly ordered and less ordered; XIV, XX: periodic and quasi-periodic vortex shedding with planar symmetry and zero mean lift; XV: slowly rotating helical regime (no regular mode) – perfectly ordered and less ordered; XVI: slow helical regime; XVII: slow helical mode with rapid oscillations with non-zero helicity; XVIII: slowly laterally oscillating helical regimes; left-pointing triangle: less ordered version of the same state.

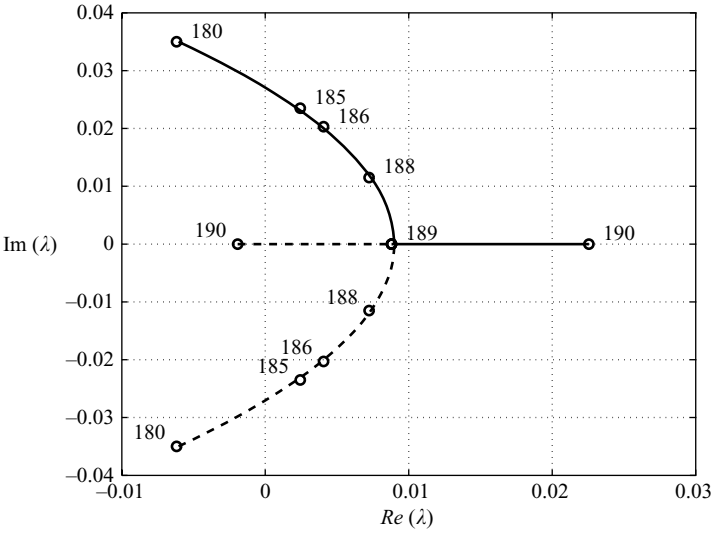

FIGURE 5. Paths of the colliding pair of complex eigenvalues giving rise to a pair of real eigenvalues. The path is parameterized at $Ri = -0.1$ and $Re \in [180, 190]$. The points obtained by linear analysis are represented by circles and are labelled by the corresponding Reynolds number value.

5. General remarks on the method of investigation of parameter planes and on the visualization of results

The following sections describe the three-dimensional flow patterns evidenced when sweeping the two Ri–Re parameter planes or, more accurately, four half-planes ($Ri > 0$ and $Ri < 0$). The method of investigation of the scenario of transition to turbulence is that of varying the Reynolds number at a constant Richardson number: at a fixed Ri, we increased the Reynolds number up to $Re = 1400$ at $Pr = 0.72$ and up to $Re = 600$ at $Pr = 7$, the highest Richardson numbers investigated being $Ri = 0.7$ ($Pr = 0.72$) and $Ri = 0.3$ ($Pr = 7$). As already explained, the limits of the investigated domains were largely given by the CPU costs. Let us remark that the latest stages of transition at high Ri and Re require not only much higher spatial resolution and thus higher computing costs per unit time scale but, more importantly, also present complicated dynamics, the analysis of which demands very long runs over very many time units. It is worth mentioning that the investigation of such regimes at $Pr = 0.72$ and $Ri \geqslant 0.4$, $Re \geqslant 1000$ took about 90 % of the overall CPU time spent on the simulations in this parameter plane and that it was outright prohibitive to tackle the investigation beyond $Re = 600$ in the $Pr = 7$ parameter plane.

In three-dimensional simulations, the number of azimuthal modes taken into account adds an additional parameter to those mentioned in table 1. In agreement with the theoretical considerations of Ghidersa & Dušek (2000), the decrease of azimuthal modes depending on the azimuthal wavenumber is exponential. (We verified that the decrease of modes measured in terms of their energy is actually very close to exponential even for 11 modes.) For many three-dimensional simulations, testing showed that four azimuthal modes (0 to 3) provided a satisfactory accuracy. Nevertheless, as Ri and Re increase, the flow presents more complicated structures in the azimuthal direction, and the number of azimuthal modes taken into account has to be raised. All the simulations of the 'stiff' regimes ($Ri \geqslant 0.4$ and $Re \geqslant 1000$ at

$Pr = 0.72$ and $Ri = 0.3$ and $Re \geqslant 500$ at $Pr = 7$) were performed with seven azimuthal modes.

The classification of observed regimes, briefly described in the legends of figures 2 and 4, distinguishes regimes characterized by specific dynamics. The roman numbering is intended to facilitate references to figures and explanatory text.

Before proceeding with the description of the various regimes there remains to explain the method of flow visualization used throughout the paper. A summarizing and often sufficient information is provided by the hydrodynamic force. We use the non-dimensionalized vector (treated as a three-component vector $\boldsymbol{C}_{h.f.} = (C_x, C_y, C_z)$), defined as

$$\boldsymbol{C}_{h.f.} = \frac{\boldsymbol{F}}{\frac{1}{2}\rho v_\infty^2 \frac{\pi d^2}{4}}, \tag{5.1}$$

where $\boldsymbol{F}$ is the total hydrodynamic force acting on the sphere. In what follows, $C_x \equiv C_D$ will be referred to as drag coefficient and the remaining two-component vector (C_y, C_z) as a lift coefficent, the norm of which will be denoted C_L. The plots of (C_y, C_z) provide good information on the transitional states. To provide exhaustive information on the flow itself would consists in describing all the computed fields: three velocity components, pressure and temperature. Plotting isosurfaces of quantities has become a common visualization method even though a single isosurface is far from reflecting the whole three-dimensional reality. Even so, it is impractical to represent all computed fields for the many regimes evidenced at the transition. It is thus sufficient to choose one of them, possibly that which suits best for discerning the most important features of the flow, such as axial vorticity. Its most obvious advantage consists in the fact that it is zero for axisymmetric flow and that it reveals the shed vortices. The method of Jeong & Hussain (1995) yielding almost equivalent plots is also sometimes used for comparison.

All the presented plots focus on the asymptotic regimes; i.e. in many cases the transients have been truncated. Especially at the ultimate stages of transition, the attractors are only very marginally stable, and the transients are very long to disappear. Conversely, the attractors become only very weakly unstable if the regime changes. To save (weeks of) CPU time, we proceeded both ways, from more to less ordered states and back, to obtain each time a weak and a strong perturbation of the investigated attractor. In the same time, such an approach provides a relatively reliable means of detecting hysteretic behaviour (see e.g. Jenny *et al.* 2004). In this work we found no case of hysteresis.

6. Regimes of a weakly heated sphere wake

At the start of our investigation, we expected to find the same scenario as the one typical for an unheated sphere wake just shifted to higher and lower Reynolds numbers for assisting and opposing flows, respectively. This conjecture was verified only in a very limited domain along the $Ri = 0$ axis. The domain is almost triangular on the opposing flow side (figure 4), delimited roughly by a straight line connecting the junction of the regular and Hopf bifurcations to the threshold of a chaotic flow at $Ri = 0$ and $Re = 360$. On the assisting flow side (figure 2) it is cut off by the vertical line of stable steady states transiting directly to chaos at $Ri = 0.3$ evidenced at $Pr = 0.72$. The regimes in this zone have the same characteristics for opposing and assisting flows, therefore we reserve a special section for them.

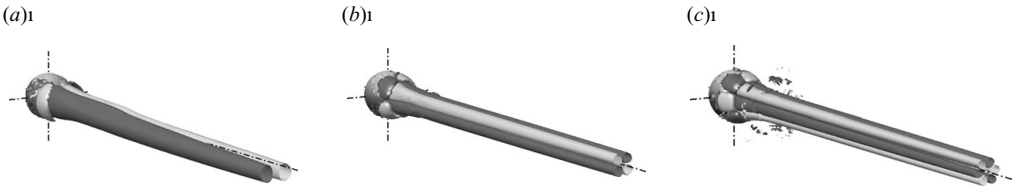

FIGURE 6. Three types of steady flow. Isosurfaces of axial vorticity at $Pr = 0.72$. (*a*) Regime I: bifid wake with symmetry plane at $Ri = 0.2$ and $Re = 400$; $\omega_x = \pm 0.1$. (*b*) Regime II: wake with four vorticity threads and two symmetry planes at $Ri = 0.6$ and $Re = 1100$; $\omega_x = \pm 0.01$. (*c*) Regime III: wake with six vorticity threads and three symmetry planes at $Ri = 0.7$ and $Re = 1300$; $\omega_x = \pm 0.001$.

The transition in the wake of an unheated sphere proceeds via three widely known stages: a steady non-axisymmetric regime, a periodic oscillating regime (see Natarajan & Acrivos 1993; Johnson & Patel 1999; Ghidersa & Dušek 2000) and a quasi-periodic regime (Mittal 1999; Bouchet *et al.* 2006). The quasi-periodic regime appears as a precursor of the transition to chaos in many configurations such as a cylinder (Thompson, Hourigan & Sheridan 1996) and a normal flat plate (Najjar & Balachandar 1996; Wu *et al.* 2005).

6.1. *Steady flow with two contra-rotating vorticity threads and a symmetry plane (I)*

Similar to the case of an unheated sphere, a steady wake with two contra-rotating vorticity threads shifted off the flow axis and keeping a plane of symmetry is the first pattern that the flow assumes when the axisymmetry is broken. The bifid aspect of the wake is due to the wavenumber $m = 1$ (periodicity of 2π and opposite signs of the vorticity threads) of the most unstable azimuthal mode at the threshold of three-dimensionality. The $m = 1$ subspace was found to be the most unstable up to $Ri = 0.590$ at $Pr = 0.72$ and for all Ri investigated at $Pr = 7$. The upper limit found at $Pr = 0.72$ was determined by an accurate linear analysis. Such a flow presents a non-zero lift coefficient. The aspect of the flow is shown in figure 6(*a*) (isosurfaces of axial vorticity) for $Ri = 0.2$, $Re = 400$ and $Pr = 0.72$. Note that for axisymmetric flows the axial vorticity is zero, which makes the axial vorticity a convenient quantity to visualize while describing axisymmetry breaking. The isosurface of temperature in the same regime is represented in Kotouč *et al.* (2008).

6.2. *Periodic vortex shedding with planar symmetry and non-zero mean lift (II)*

The secondary (Hopf) bifurcation, due to a nonlinear excitation of a complex eigenpair of the same $m = 1$ subspace by the already-developed steady mode makes the bifid wake oscillate periodically while keeping the formerly chosen symmetry plane. The periodic wake found at $Ri \leqslant 0.2$ at $Pr = 0.72$ and $Pr = 7$ exhibits the typical periodic vortex shedding. The bifid wake being shifted off the flow axis in the three-dimensional steady regime, the average position of the oscillating vorticity threads after the onset of the secondary bifurcation is shifted too, and the average lift force is thus non-zero. The lift coefficient, as well as other quantities in the wake, presents a periodic behaviour characteristic of a limit cycle. To illustrate the flow pattern, the axial vorticity isosurfaces (figure 7*a*) and the visualization of vortical structures by the method of Jeong & Hussain (1995) (figure 7*b*) are plotted at $Pr = 7$, $Ri = 0.1$ and $Re = 400$. The wake presents a characteristic vortex street with alternate vortices of opposite axial vorticity sign.

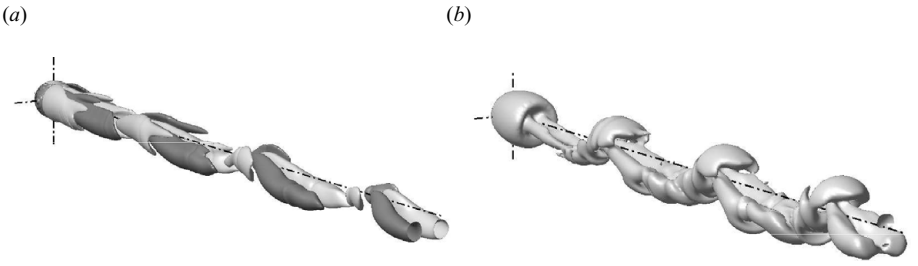

FIGURE 7. Snapshots of the flow pattern at two instants differing by a half of a period at $Ri = 0.1$, $Re = 400$ and $Pr = 7$. (*a*) Isosurfaces of axial vorticity at the levels $\omega_x = \pm 0.1$. (*b*) Vortical structures – the Q-definition (see Jeong & Hussain 1995) – at the level $Q = 0.001$. The flow presents a vortex street of alternate vortices, the symmetry plane being that of the three-dimensional steady regime.

Pr	*Ri*	*Re*	*St*	*Pr*	*Ri*	*Re*	*St*	*Pr*	*Ri*	*Re*	*St*
0.72	0	300	0.135	0.72	0.2	850	**0.218**	0.72	0.55	1000	7.26×10^{-3}
0.72	0	350	**0.130**	0.72	0.4	1000	0.058	0.72	0.58	1200	0.038
0.72	0.1	400	0.163	0.72	0.4	1050	0.060	0.72	0.58	1300	0.043
0.72	0.1	450	0.167	0.72	0.4	1000	0.058	0.72	0.6	1200	0.037
0.72	0.1	500	0.168	0.72	0.4	1050	0.060	0.72	0.6	1300	0.044
0.72	0.1	550	**0.164**	0.72	0.4	1100	**0.059**	7	0	300	0.135
0.72	0.2	600	0.201	0.72	0.4	1200	**0.058**	7	0	350	**0.130**
0.72	0.2	650	0.202	0.72	0.5	1000	7.98×10^{-3}	7	0.1	400	0.149
0.72	0.2	700	0.206	0.72	0.5	1100	8.02×10^{-3}	7	0.1	450	0.149
0.72	0.2	750	**0.207**	0.72	0.5	1200	8.19×10^{-3}	7	0.1	500	**0.141**
0.72	0.2	800	**0.208**	0.72	0.5	1300	8.35×10^{-3}	7	0.2	600	0.169

TABLE 4. Assisting flow: Strouhal numbers for all periodic and quasi-periodic (shown in bold) regimes evidenced at both Prandtl numbers.

The value of Strouhal number is defined as

$$St = \frac{f d}{u_\infty}, \tag{6.1}$$

where f is the frequency of the periodic wake oscillations. It increases with Re at constant Ri and Pr and, similarly, it increases with Ri at constant Re and Pr. At constant Ri and Re, the Strouhal number decreases with Pr. Tables 4 and 5 sum up Strouhal numbers for all periodic and quasi-periodic (with the frequency corresponding to the highest peak in the frequency spectrum being given) regimes evidenced. Note that for a non-heated sphere, the Strouhal number at the onset of the Hopf bifurcation at $Re_2 = 272$ is $St = 0.127$ (see Johnson & Patel 1999; Bouchet *et al.* 2006). In what follows we understand the Strouhal number as any frequency f non-dimensionalized using (6.1); i.e. we refer to (6.1) even for regimes presenting oscillations without vortex shedding.

A truncation of the azimuthal decomposition to $m = 0$ and $m = 1$ modes affects only very weakly the found solution. The latter remains oscillating with only a slightly smaller amplitude and a slightly greater mean value of the lift. The essential dynamics are thus related to the $m = 1$ subspace. The higher modes play merely the role of slave modes.

Pr	*Ri*	*Re*	*St*	*Pr*	*Ri*	*Re*	*St*	*Pr*	*Ri*	*Re*	*St*
0.72	0	300	0.135	0.72	−0.11	210	9.33×10^{-2}	7	0	300	0.135
0.72	−0.03	290	0.126	0.72	−0.12	185	8.82×10^{-2}	7	−0.05	240	0.119
0.72	−0.05	240	0.115	0.72	−0.12	200	9.05×10^{-2}	7	−0.05	270	0.127
0.72	−0.05	270	0.119	0.72	−0.13	175	8.48×10^{-2}	7	−0.1	210	0.105
0.72	−0.05	290	0.115	0.72	−0.13	185	8.77×10^{-2}	7	−0.1	230	0.113
0.72	−0.07	250	0.109	0.72	−0.13	200	8.96×10^{-2}	7	−0.11	220	0.108
0.72	−0.07	260	0.107	0.72	−0.15	170	8.40×10^{-2}	7	−0.11	230	0.112
0.72	−0.08	240	0.106	0.72	−0.2	140	7.90×10^{-2}	7	−0.15	175	9.38×10^{-2}
0.72	−0.09	212	0.102	0.72	−0.2	170	7.98×10^{-2}	7	−0.15	190	0.100
0.72	−0.09	220	0.103	0.72	−0.2	190	9.37×10^{-2}	7	−0.17	190	9.69×10^{-2}
0.72	−0.09	230	0.102	0.72	−0.23	170	9.17×10^{-2}	7	−0.2	150	8.90×10^{-2}
0.72	−0.1	200	9.41×10^{-2}	0.72	−0.25	100	6.84×10^{-2}	7	−0.2	170	9.47×10^{-2}
0.72	−0.1	210	9.83×10^{-2}	0.72	−0.25	125	7.99×10^{-2}	7	−0.2	180	9.54×10^{-2}
0.72	−0.11	200	9.33×10^{-2}	0.72	−0.25	150	8.79×10^{-2}	7	−0.25	125	8.43×10^{-2}
								7	−0.25	150	9.22×10^{-2}

TABLE 5. Opposing flow: Strouhal numbers for all periodic regimes at both Prandtl numbers. The Strouhal numbers of quasi-periodic planar and three-dimensional regimes are close to the values of periodic regimes situated in the vicinity of the quasi-periodic regimes in the *Ri*–*Re* diagram of figure 4.

The convection (increasing Richardson number) tends, at first, not only to push the Hopf bifurcation threshold to higher Reynolds numbers but also to widen the interval of the limit cycle stability until the existence of the regime is abruptly cut off at $Ri = 0.3$.

6.3. *Quasi-periodic flow with planar symmetry, vortex shedding and non-zero mean lift (III)*

The periodic vortex shedding evidenced for $Ri < 0.3$ at both considered Prandtl numbers was systematically found to undergo a second Hopf bifurcation bringing about a second, incommensurate, frequency and yielding limit torus dynamics. (At $Pr = 7$, the parameter domain did not extend high enough to evidence the quasi-periodic regime at $Ri = 0.2$.) The symmetry plane remains conserved. Figure 8 shows the time evolution of the lift coefficient and its frequency spectrum at $Ri = 0.1$, $Re = 500$ and $Pr = 7$. Figure 9 shows the corresponding flow aspect. (For this simulation, the computational domain was extended downstream to $L_{out}/d = 60$ to represent the largest length scale of the flow within the computation domain.) Note the local vortex street extinction at $x/d \approx 25$ downstream of the sphere. This extinction is a fingerprint of the lift extinction occurring with a periodicity of 50 time units in figure 8(*a*).

7. Three-dimensional regimes specific for assisting flow

The investigation of the $Pr = 7$ plane was too limited to reveal ordered regimes specific for assisting flow (distinct from those described in §6). The following description concerns thus only the case of $Pr = 0.72$, although a similar behaviour can be conjectured in the $Pr = 7$ case.

7.1. *Steady three-dimensional flows*

As we already mentioned, with increasing Richardson number, we observe three distinct cases depending on the azimuthal subspace in which the primary instability

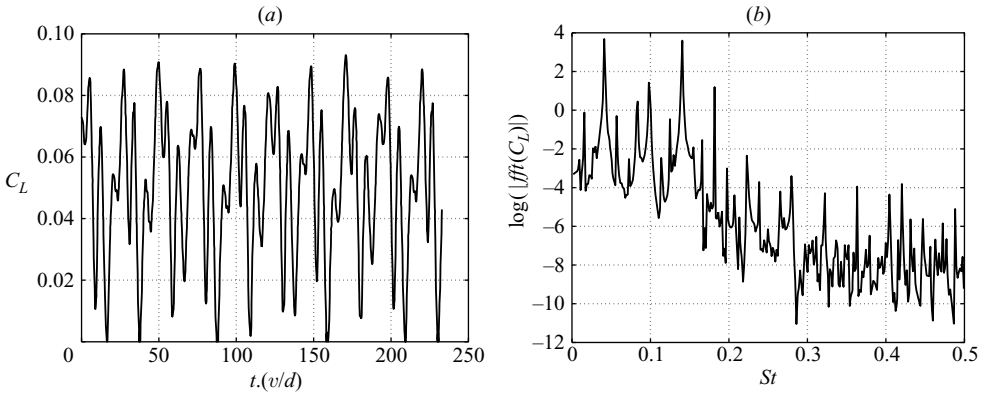

FIGURE 8. (*a*) Time evolution of the lift coefficient of quasi-periodic oscillations at $Ri = 0.1$, $Re = 500$ and $Pr = 7$; (*b*) the corresponding power spectrum. The dominant Strouhal number is 0.141; the most important sub-harmonic frequency corresponds to the Strouhal number $St = 0.041$.

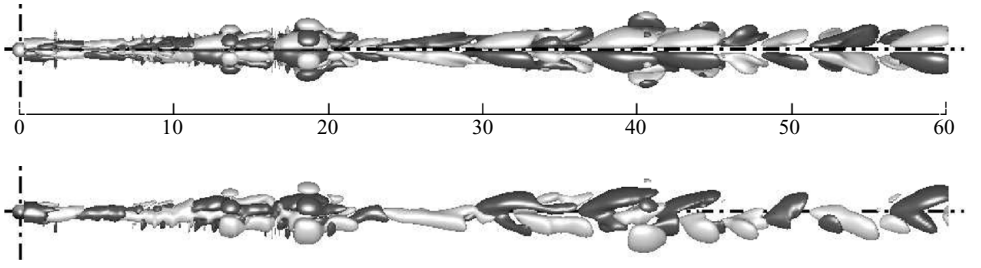

FIGURE 9. Isosurfaces of axial vorticity at the levels $\omega_x = \pm 0.02$ viewed along (up) and perpendicular to (bottom) the symmetry plane at $Ri = 0.1$, $Re = 500$ and $Pr = 7$. The symmetry plane is conserved, but the vortex shedding presents extinctions that can be associated with lift oscillation extinctions visible in figure 8(*a*).

sets. Farther inside the three-dimensional domain (above the primary-instability line) several azimuthal modes are significant, and the distinction between cases when one of them is dominant becomes very rapidly unclear. The regime with two vortex threads was described in § 6.1

7.1.1. *Steady flow with four vorticity threads and two perpendicular symmetry planes (IV)*

If the wavenumber of the most unstable azimuthal mode at the threshold of the loss of axisymmetry is $m = 2$ (for $0.590 \leqslant Ri \leqslant 0.714$ at $Pr = 0.72$) the flow pattern presents four steady vorticity threads and two perpendicular symmetry planes. At $Pr = 0.72$, the limits of this type of instability expressed in terms of Richardson numbers were found to be $0.590 \leqslant Ri \leqslant 0.714$. The flow has a period of π in the azimuthal direction, and the resulting lift is thus zero because it integrates only effects of the $m = 1$ mode (see Jenny & Dušek 2004). The aspect of the flow with four vorticity threads is shown in figure 6(*b*) for $Ri = 0.6$, $Re = 1100$ and $Pr = 0.72$. The unstable mode is very weak, and, though very well representable in terms of axial vorticity, it is not visible on a plot of a temperature isosurface.

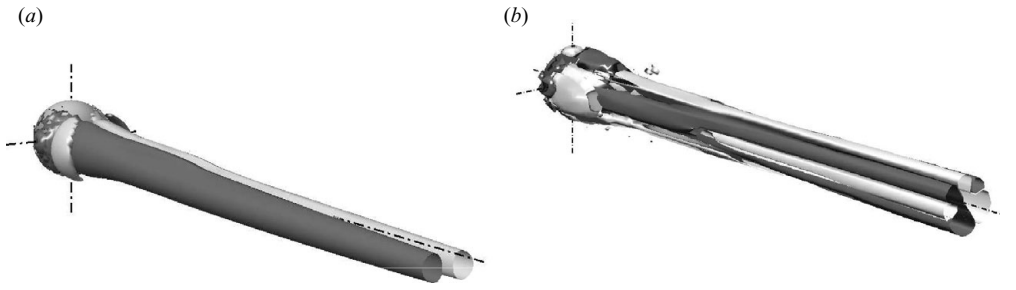

FIGURE 10. Isosurfaces of axial vorticity at $Pr = 0.72$. (*a*) $Ri = 0.2$ and $Re = 400$; $\omega_x = \pm 0.01$. (*b*) $Ri = 0.3$ and $Re = 1000$; $\omega_x = \pm 0.01$.

7.1.2. *Steady flow with six vorticity threads and three symmetry planes (V)*

The instability in the $m = 3$ subspace, occurring for $Ri \geqslant 0.714$ at $Pr = 0.72$, yields a flow pattern presenting six steady vorticity threads and three symmetry planes. The subdomains dominated by $m = 2$ and $m = 3$ modes extend rather parallel to the Ri axis. When the domain was swept in the Re-axis direction (at constant values of Ri) the $m = 2$ mode was observed to give way, at a higher Reynolds number, to the $m = 3$ mode.

The flow being periodic with the periodicity of $2\pi/3$ in the azimuthal direction, the resulting lift is again zero. The aspect of the flow with six vorticity threads is shown in figure 6(*c*) at $Pr = 0.72$, $Ri = 0.7$ and $Re = 1300$.

7.1.3. *Strongly supercritical steady non-axisymmetric regimes*

The regimes concerned by the present subsection resemble qualitatively those described in § 6.1. The lift is non-zero and constant; two counter-rotating vortices dominate the wake, in spite of two or four strong secondary vortex pairs. Most intriguing is rather the fact that at $Ri = 0.3$ and $Ri = 0.45$ no unsteady regime was found until the onset of chaos.

The regimes represented in figure 6 are prototypical monomodal states in which the visible mode is accompanied only by its higher harmonics. For example the flow at $Ri = 0.6$ and $Re = 1100$ contains absolutely no odd modes; only the mode $m = 2$ and its multiples are present. Similarly, the flow represented in figure 6(*a*) contains only weak higher harmonics that have no dynamics of their own and are sustained by the fundamental unstable mode via nonlinear couplings. Even represented by isovorticity surfaces at a much lower level (see figure 10*a*) the $m > 1$ modes remain invisible. On the contrary, highly supercritical flows contain clearly several vortex tubes (figure 10*b*).

What complicates the understanding of highly supercritical, albeit steady, regimes is the fact that there is no clear manner to distinguish pure higher harmonics of an unstable mode in the $m = 1$ subspace from interactions with (nearly) unstable modes in $m > 1$ subspaces. The only case in which this interaction can clearly be evidenced is when a flow containing only multiples of a given $m > 1$ mode undergoes a (spatial) subcritical bifurcation triggering the missing modes. This happens e.g. when, at $Ri = 0.6$, the Reynolds number is increased from 1100 to 1200 or, at $Re = 1300$, when the Richardson number is decreased from 0.65 to 0.6. In both cases the onset of lower azimuthal wavenumbers is accompanied by an onset of oscillations. If e.g. at $Ri = 0.6$ and $Re = 1200$, we do not include odd modes into the azimuthal Fourier decomposition the oscillations do not appear.

To investigate more closely these couplings we carried out several numerical experiments consisting of keeping only even modes in the azimuthal decomposition (case 1) on one hand and only $m = 0, 1$ modes (case 2) on the other hand. In both cases the reduced equations remain nonlinear. In the first case only perturbations driven by the $m = 2$ subspace (and their higher harmonics) are present; in the latter case, only the $m = 1$ perturbations are allowed. The test was applied to the following points of the Ri–Re plane: (0.2, 550), (0.3, 500), (0.3, 1000) and (0.45, 1300); the test was applied as well to points corresponding the three unsteady regimes: (0.2, 700), (0.4, 1050) and (0.5, 1100).

The steady non-axisymmetric regimes for $Ri = 0.2$, $Re = 550$ and $Ri = 0.3$, $Re = 500$ disappear if only even modes are retained in the azimuthal decomposition and are only weakly affected by the truncation to $m = 0, 1$. They correspond well to the steady non-axisymmetric regime in the $m = 1$ subspace of § 6.1. The stability of the steady non-axisymmetric regimes at high Reynolds numbers at $Ri = 0.45$ is explained by an equilibrium of instabilities in subspaces $m = 1$ and $m = 2$ because if only even modes are retained, a periodic oscillating regime with a plane of symmetry results this time in the $m = 2$ subspace (i.e. with zero mean lift – see § 7.2.1), whereas if the azimuthal decomposition is truncated at $m = 1$ a periodic regime without symmetry plane (with lift oscillation perpendicular to mean lift direction) is found. As for the absence of periodic oscillations at $Ri = 0.3$, the test shows that the regime is unaffected by the presence of even modes. The steady non-axisymmetric regime in the $m = 1$ subspace is exceptionally stable by itself. The nonlinear coupling inhibits the already-existing oscillations in the $m = 2$ subspace.

7.2. *Periodic regimes with planar symmetry*

The periodic regimes with planar symmetry were found to be also of three distinct types depending on the primary azimuthal subspace. The limit of the vortex shedding typical for the unheated sphere is materialized by the $Ri = 0.3$ line at which the oscillations disappear. At this Richardson number the steady regime, stable until $Re = 1000$, becomes directly chaotic at $Re = 1100$. The other two 'islands' of periodic states with planar symmetry were found at $Ri = 0.4$ and $Ri = 0.58$ and 0.6. They present significantly different characteristics.

7.2.1. *Slow periodic oscillation of two vortex threads (VI)*

The major distinctive feature of the periodic oscillations of the bifid wake at $Ri = 0.4$ (and at $Pr = 0.72$) is that the flow pattern does not exhibit the alternate vortices and that the period of the oscillations is almost four times longer as compared to the regime described in the previous subsection. The flow pattern is illustrated in figure 11. Two snapshots of the flow at two instants differing by a half period are represented. The isosurfaces of axial vorticity (figure 11a, b) represent vortex tubes exhibiting only a barely visible undulation. The amplitude (denoted $C_{L,a}$ – note that the compared regimes are perfectly periodic) of the lift coefficient is about twice smaller than at $Ri = 0.2$, $Re = 700$ ($C_{L,a} = 5.8 \times 10^{-3}$ at $Ri = 0.4$, $Re = 1000$ against $C_{L,a} = 9.3 \times 10^{-3}$ at $Ri = 0.2$, $Re = 700$). Also the mean lift is smaller ($C_{L,m} = 3.3 \times 10^{-2}$ at $Ri = 0.4$, $Re = 1000$ against $C_{L,m} = 4.8 \times 10^{-2}$ at $Ri = 0.2$, $Re = 700$). The Strouhal numbers are much smaller than for the regimes with shed vortices (see table 4).

Another important feature is the presence of two relatively strong (note the level of the vorticity isosurfaces of the figure) secondary vortex tubes (four tubes altogether) witnessing a strong $m = 2$ mode. The numerical test presented in § 7.1 yields, surprisingly, a steady axisymmetric solution if only even modes are retained. If the azimuthal expansion is truncated only to $m = 0, 1$, surprisingly again, the

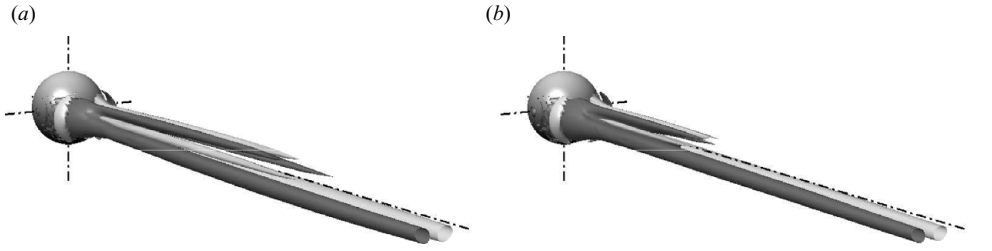

FIGURE 11. Isosurfaces of the axial vorticity at the levels $\omega_x = \pm 0.3$ at two instants differing by a half of a period, $Ri = 0.4$, $Re = 1000$ and $Pr = 0.72$ (VI). The two threads oscillate with a low amplitude, and the vortical structures no longer change sign periodically in the downstream direction – no vortex shedding is present in the flow.

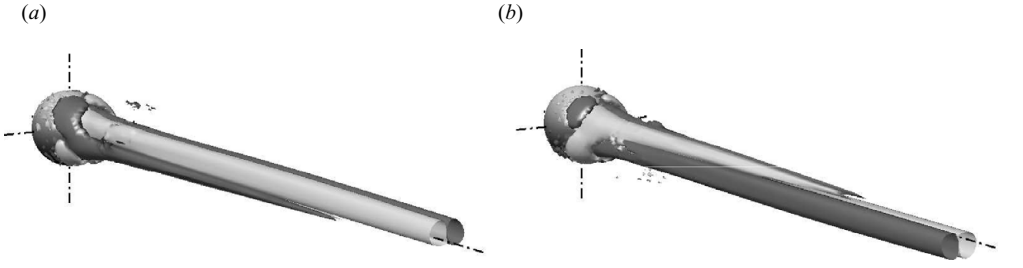

FIGURE 12. Isosurfaces of the axial vorticity at the levels $\omega_x = \pm 0.02$ at two instants differing by a half of a period of the flow at $Ri = 0.6$, $Re = 1200$ and $Pr = 0.72$ (VII). The four threads oscillate parallel to one and perpendicularly to the other of the symmetry planes established in the steady regime.

slowly rotating regime (IX) described in § 7.3.1 is obtained. Even if the regimes obtained in the test were unexpected the result of the tests confirms the expectation that the interaction of both subspaces $m = 1$ and $m = 2$ is necessary to sustain the oscillations. The mode $m = 1$ remains, however, still dominant. In contrast to the vortex shedding described in the previous subsection, the resulting Hopf bifurcation has to be understood as resulting from a fully nonlinear and three-dimensional state of the flow without direct relation to any of the eigenvalues of the axisymmetric flow.

7.2.2. *Quasi-periodic flow with planar symmetry without vortex shedding (VIII)*

This flow regime is the next transition stage of the periodic regime described in § 7.2.1 in the same way as the quasi-periodic regime III is related to regime II. The flow aspect is very similar to that of figure 11. The undulation of the vortex threads is significantly stronger, but alternate vortex shedding is absent. The common feature of the quasi-periodic regimes is that the dominant frequency remains that of the associated periodic flow. In this case the secondary Strouhal number is about three times smaller as compared to that of the related periodic regime.

7.2.3. *Slow periodic oscillations of four vortex threads with a plane of symmetry (VII)*

Unlike in the previous case ($Ri = 0.4$), the two periodic regimes evidenced at $Re = 1200$ and $Ri = 0.58$ and 0.6 present a zero mean lift. The lift is, nevertheless, non-zero and oscillates about the zero mean value in one of the two symmetry planes established at the primary instability, which sets in the $m = 2$ subspace. A pair of the vortex threads becomes alternately stronger than the other during a period of oscillations; both remain equal in the average (see figure 12). The numerical test of § 7.1 shows that the oscillations disappear in the absence of odd modes. A truncation

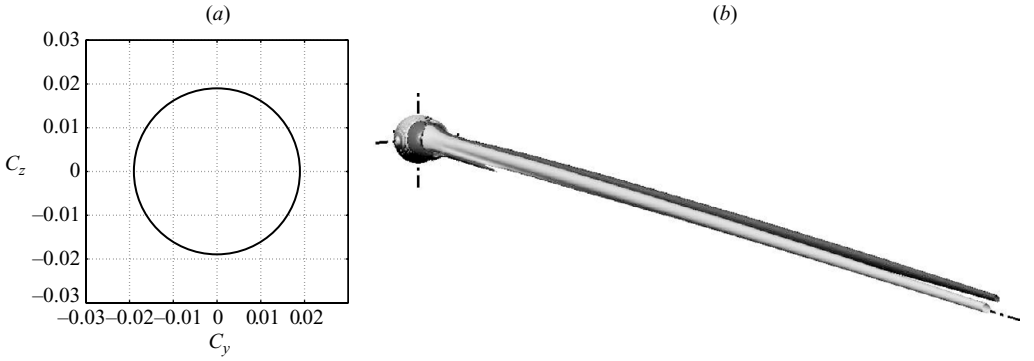

FIGURE 13. (*a*) Projection of the lift coefficient onto the plane perpendicular to flow axis at $Pr = 0.72$, $Ri = 0.5$ and $Re = 1100$ (IX). (*b*) Isosurfaces of axial vorticity at the levels $\omega_x = \pm 0.2$. Note the twisted vortex threads resulting from the rotation of the symmetry plane.

to $m = 0,\ 1,\ 2$ modes leaves the oscillations unaffected. This means that the mode $m = 2$ is dominant but that the interaction of $m = 1$, $m = 2$ subspaces is necessary to sustain the oscillations. The interaction with the $m = 3$ subspace has negligible effects. The amplitude of the lift coefficient was found to be 6.4×10^{-3} and the Strouhal number 0.037 at $Re = 1200$ and $Ri = 0.6$.

7.3. *Ordered states without symmetry plane*

Higher order nonlinear effects tend to break the remaining symmetry plane. This change is very rapid in terms of the Reynolds number variation for low Richardson numbers and is perceived as a direct transition to chaos with the coarse Reynolds number step of diagram 2. At $Pr = 0.72$, many, more or less ordered, regimes were obtained at values of Ri greater than or equal to 0.4. Namely, at $Ri = 0.5$ and $Ri = 0.55$, an intriguing periodic slow rotation of the vorticity threads around the flow axis was found for Reynolds numbers ranging from 1000 to 1300. A different periodic rotating regime, dominated by an $m = 3$ mode was found at $Ri = 0.58$ and $Ri = 0.6$ at $Re = 1300$. All other regimes have more or less complicated non-periodic dynamics preceding very likely a transition to full chaos.

7.3.1. *Two slowly rotating vorticity threads (IX)*

At $Pr = 0.72$, $Ri = 0.5$ and for $1000 \leqslant Re \leqslant 1300$ and at $Ri = 0.55$ and for $Re = 1000$, the steady vorticity threads were observed to form a slowly turning spiral corresponding to a slow rotation of the initial symmetry plane. As a result, the projection of the lift coefficient onto the plane perpendicular to the flow axis has the form of a circle (see figure 13*a*). The circle is perfect at its onset at $Re = 1000$ – with no higher harmonics in the time behaviour. Later on, at $Re = 1200$, the dynamics of the flow begin to be modulated by higher harmonics. The Strouhal number at this regime is extremely low (see table 4); the period is 25 times longer than that of the regime with vortex shedding and 6 times longer than the periodic regime described in § 7.2.1. For a long time we had no reasonable explanation of the origin of this regime. A hint is now provided by the test carried out at $Ri = 0.4$ and $Re = 1050$ mentioned in § 7.2.1. The rotation obtained with the azimuthal expansion truncated to $m = 0, 1$ presents exactly the same characteristics as the regime presented in figure 13. This means that the slowly rotating regime originates essentially in the $m = 1$ subspace. The stabilizing effect of convection prevents the vortex shedding from setting in. This

extends the stability of the steady non-axisymmetric regime to Reynolds numbers exceeding 1000 (see figure 4). The convection acts mostly in the close wake. The far wake is less stable, and its symmetry plane ends up turning slowly. The role of the coupling between $m = 1, 2$ consists of delaying the onset of the regime to a higher Richardson number.

7.3.2. *Periodic regime dominated by $m = 3$ mode with rotating lift (X)*

This regime, observed at $Re = 1300$ and $Ri = 0.58, 0.6$ (at $Pr = 0.72$) can be viewed as arising from the periodic regime described in § 7.2.3 destabilized by a coupling with the $m = 3$ subspace. The resulting three-dimensional pattern presents six vorticity threads of different intensity. When represented as a movie, the threads do not rotate, unlike in § 7.3.1. Their intensity appears only to be modulated with the period of the flow. Nevertheless, the lift rotates with a Strouhal number $St = 0.044$, which can be considered a continuation of the value given in § 7.2.3.

7.3.3. *Non-periodic rotating regimes (at $Pr = 0.72$) (XI)*

These regimes represent the ultimate stage before the transition to chaos. We discriminate them from chaotic states by the absence of chaotic structures in the wake (resolved in the simulation, i.e. up to 25 diameters downstream of the sphere) and by a quasi-periodic time evolution of the lift coefficient. Their common feature consists in presenting several regular vorticity threads. (The number of dominant threads is indicated by different shading in figure 2.) Their dynamics correspond to the transition from the closest more ordered regime to chaos. That is where a symmetry plane is present it gets lost; where a periodicity is present, more complicated, possibly quasi-periodic, dynamics set in. For example the regime at $Ri = 0.4$ and $Re = 1300$ (figure 14*a*) differs from that at $Ri = 0.4$ and $Re = 1200$ because of the loss of stability of the symmetry plane resulting in slowly rotating quasi-periodic oscillations of the lift. The regimes in figure 14 (*b–d*) arise from a flow already without a symmetry plane but are characterized by the loss of periodicity.

7.4. *Chaotic flow (XII)*

'Chaotic flow' is not necessary synonymous with 'turbulent flow'. Note that chaos is widely accepted to arise in dynamical systems as a result of a single or of a rapidly converging sequence of bifurcations (e.g Strogatz 1994); it has thus a 'threshold', and unlike a 'developed turbulent flow', a chaotic flow just above its threshold cannot be expected to develop suddenly a turbulent energy spectrum. In the present case, chaotic behaviour is rather related to very long time scales. There exist mathematically well-defined criteria of chaos such as the Lyapunov exponents and the Hausdorff dimension of the strange attractor. Their practical applicability is, however, very limited. Therefore we do not claim to prove rigorously that the states described in the present sections are 'chaotic' in mathematical sense. As will be seen, they lack any spatial or temporal periodicity.

A chaotic flow presents both chaotic structures in the wake and a chaotic projection of the lift onto a plane perpendicular to the flow direction (figure 15). The computing costs needed to investigate an established chaotic behaviour close to its onset are high. For example the simulation at $Pr = 0.72$, $Ri = 0.2$ and $Re = 900$ in figure 16(*a*) corresponds to 160 periods of vortex shedding in the corresponding periodic regime (at $Re \leqslant 500$). In spite of that, the chaotic behaviour of all regimes XIV has been thoroughly checked. It might rather happen that some of the regimes considered 'ordered' in § 7.3.3 end up becoming chaotic. The thermal plume shifts, very likely, the

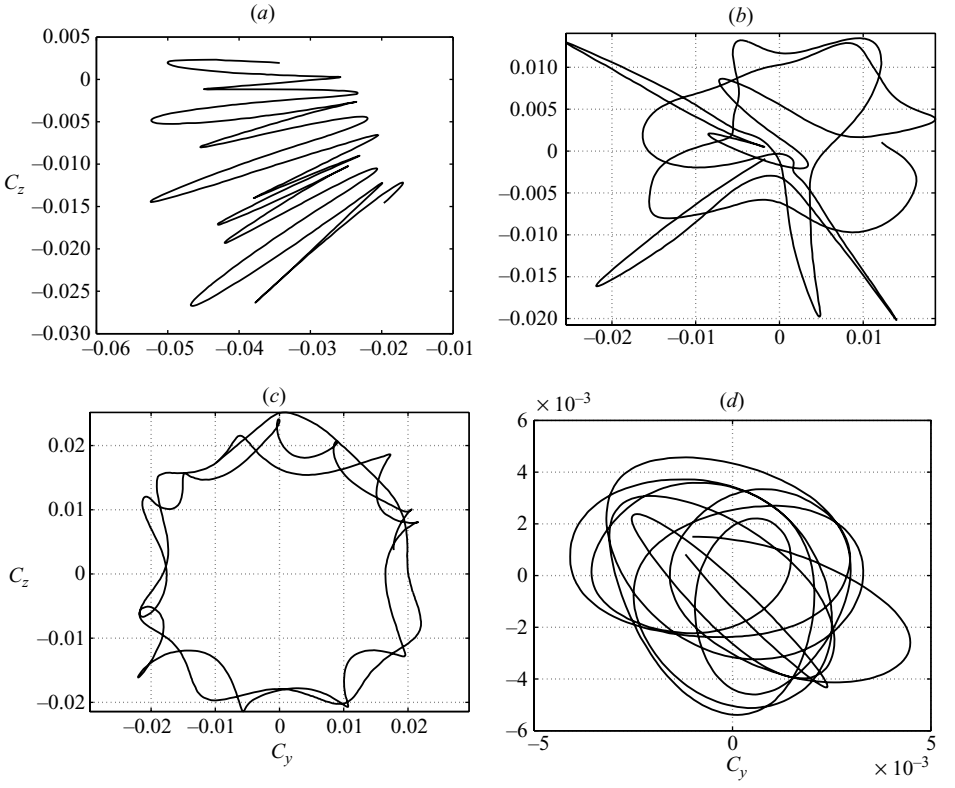

FIGURE 14. Projection of the lift coefficient onto the plane perpendicular to flow axis at $Pr = 0.72$ and (*a*) $Ri = 0.4$, $Re = 1300$; (*b*) $Ri = 0.55$, $Re = 1300$; (*c*) $Ri = 0.5$, $Re = 1400$; and (*d*) $Ri = 0.6$, $Re = 1400$ (regimes numbered XI).

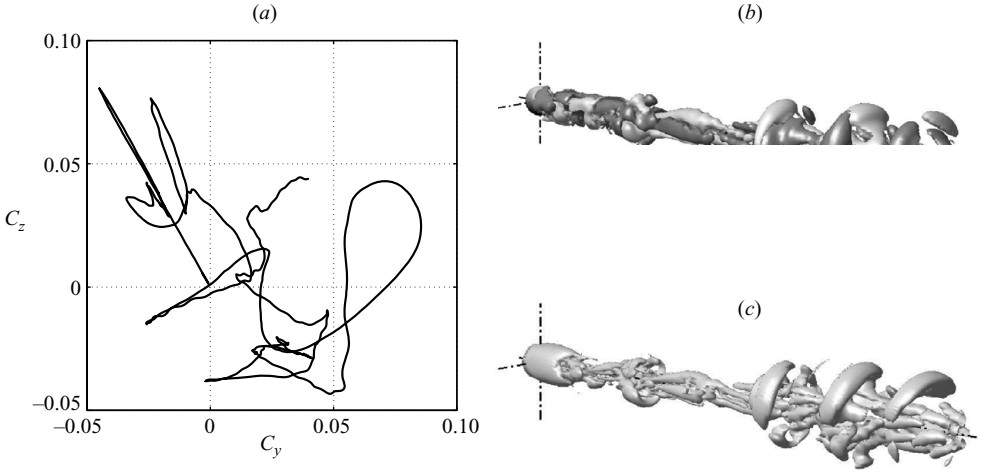

FIGURE 15. (*a*) Projection of the lift coefficient onto the plane perpendicular to flow axis; (*b*) axial vorticity at the levels $\omega_x = \pm 0.2$; and (*c*) vortical structures at the level $Q = 0.001$ at $Pr = 0.72$, $Ri = 0.1$ and $Re = 1000$ (XII). At this Richardson number the threshold of chaos lies at $Re = 600$.

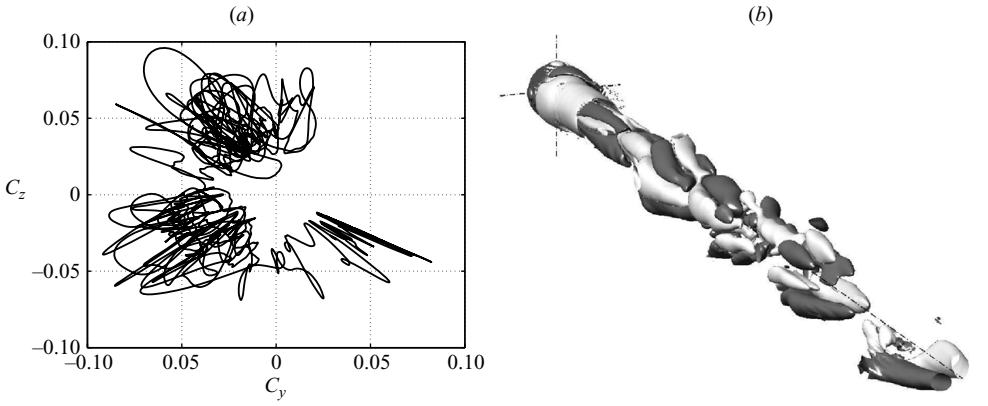

FIGURE 16. $Pr = 0.72$, $Ri = 02$, $Re = 900$. (*a*) Projection of the lift coefficient onto the plane perpendicular to flow axis. (*b*) Isosurfaces of axial vorticity at levels ± 0.15.

chaotic regime outside the investigated parameter domain, so that any clear chaos for $Ri > 0.3$ is not evidenced.

8. Three-dimensional transitional regimes specific for opposing flow

The Ri–Re parameter planes at $Pr = 0.72$ and $Pr = 7$ were scanned, again, mainly along lines in the increasing Re direction as can be seen in figure 4. Depending on the complexity of the distribution of different regimes the density of investigated points was varied. The approximate limits of subdomains corresponding to the regimes described below are represented by thin lines in figure 4. The points at which the regimes have been identified are marked by symbols described in the caption of the figure. In the direction of increasing Reynolds numbers we stopped the investigation at the onset of chaos. Due to the destabilizing effect of an increasingly strong convection, the upper bound for the threshold of onset of chaos is given by that of the unheated sphere situated close to $Re \approx 400$. The Reynolds number $Re = 350$ was sufficiently high to evidence chaos at the smallest (in absolute value), but non-zero, considered Richardson number. On the left-hand side of the parameter planes we stopped our investigation at $Ri = -0.25$ (with some excursions down to $Ri = -0.5$ at $Pr = 7$). At $Ri = -0.25$, the primary-instability threshold drops to $Re_{crit,1} \sim 100$. For both considered Prandtl numbers, the scenario of transition seems to be similar at higher (more negative) Richardson numbers. The interest of pushing the investigation further left, to more negative Richardson numbers, consists rather in the investigation of the flow reversal due to a dominant convection. At a very low Reynolds number (smaller than 1) this phenomenon raised the problem of a huge recirculation observed by Mograbi & Bar-Ziv (2005*a*). It is clear that at Reynolds numbers greater than 1, the flow reversal will occur in a chaotic and fully three-dimensional flow. The presentation of the result of investigation of this phenomenon goes, however, beyond the scope of this paper. Let us just remark that the reverse plume bringing about a change of the drag sign occurs at Richardson numbers exceeding 1 in absolute value, which lie beyond the limits of the parameter planes presented in figure 4.

The transition scenario in opposing flow is different from that of assisting flow because of the primary bifurcation of Hopf type. This fact has made it necessary to distinguish several more regimes in addition to those already described above (see figure 4). As has already been pointed out, the transition in opposing flow is driven

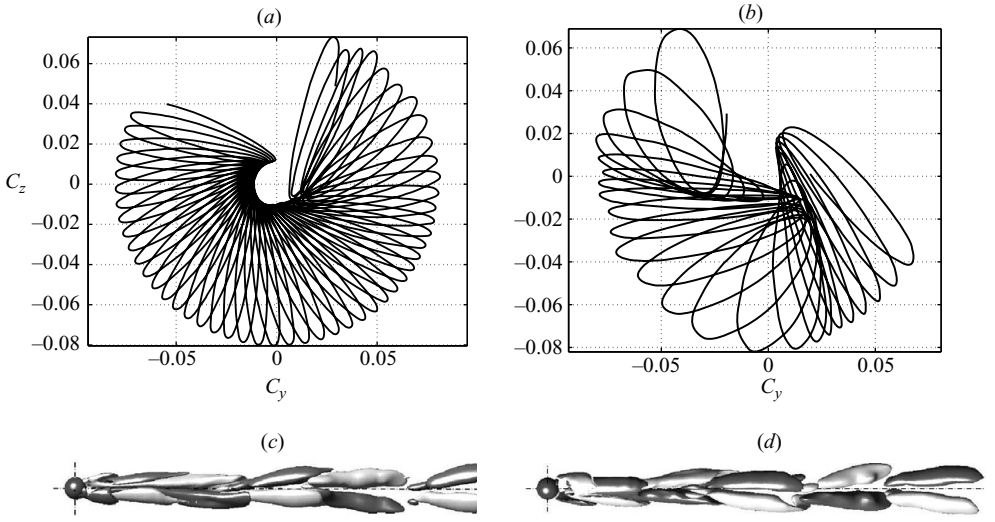

FIGURE 17. Upper figures: paths of lift coefficient; (*a*) $Ri = -0.1$ and $Re = 220$; (*b*) $Ri = -0.08$ and $Re = 260$. Lower figures: axial isovorticity surfaces at $\omega_x = \pm 0.2$; (*c*) $Ri = -0.08$ and $Re = 250$; (*d*) $Ri = -0.08$ and $Re = 260$. The view is taken along the local symmetry plane in the remote wake to show the helical distortion in the near wake (regimes XIII).

by the $m = 1$ azimuthal subspace. The dynamics of the $m = 1$ subspace being perfectly represented by the lift, we use mainly the lift coefficient vector (5.1) to characterize the different regimes. The lift coefficient plots are illustrated in some cases by the three-dimensional vorticity plots representing the vorticity structures in the wake.

8.1. *Low Richardson numbers*

In this subsection we focus on specific ordered regimes that appear before the originally periodic flow with planar symmetry and non-zero mean lift (II) becomes chaotic.

8.1.1. *Oscillating regime without symmetry plane and slowly rotating mean lift (XIII) at* $Pr = 0.72$

Opposing flow is characteristic for its earlier loss of planar symmetry as compared to an unheated sphere wake. At the moderate Prandtl number $Pr = 0.72$, the symmetry plane looses easily its stability, and higher order effects set in before the dynamics of the second eigenpair start to be visible. At Prandtl number $Pr = 7$, the planar symmetry appears to be much more robust, and the quasi-periodic regime with planar symmetry and non-zero mean lift exists along the whole upper limit of the periodic regime.

The most ordered regime mixes one pair of helical modes with the steady eigenmode responsible for the non-zero mean lift. The non-zero helicity, appearing as a spiralling path of the lift coefficient, is due to a non-perfect equilibrium of the helical modes associated with the complex eigenpair, which is at the origin of the periodic regime with planar symmetry (II). The loss of symmetry with respect to the change of the helicity sign was explained in Danaila, Dušek & Anselmet (1998) by higher nonlinear effects. This regime is relatively hard to find because it is confined to a very narrow strip along the upper limit of the subdomain corresponding to the periodic regime (II). Three cases, at $Ri = -0.07$ and $Re = 270$, at $Ri = -0.08$ and $Re = 250$ and at $Ri = -0.1$ and $Re = 220$ have been evidenced (see figure 17*a*). In the diagram in

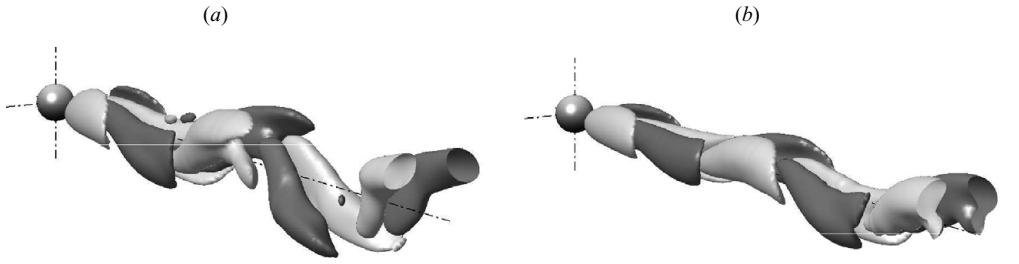

FIGURE 18. Periodic vortex shedding with zero mean lift (*a*) at $Pr = 0.72$, $Ri = -0.25$ and $Re = 125$ and (*b*) at $Pr = 7$, $Ri = -0.2$ and $Re = 150$, represented in terms of axial isovorticity surfaces at (*a*) $\omega_x = \pm 0.3$ and (*b*) $\omega_x = \pm 0.1$ (regimes XIV).

figure 4 they are represented by a filled circle. Elsewhere (small filled circle inside a larger one) in figure 4) a secondary frequency is present (see figure 17*b*). The three-dimensional plots show clearly the absence of the symmetry plane due to the helical torsion of the wake structures (figure 17*c*, *d*).

8.2. *Higher Richardson numbers*

At $Pr = 0.72$ and Richardson numbers below -0.2 the transition scenario no longer qualitatively varies with the Richardson number value. A similar trend was observed at $Ri \sim -0.5$ and $Pr = 7$. Here we describe in detail what happens if the line $Ri = -0.2$ is swept at $Pr = 0.72$.

The primary Hopf bifurcation yields a periodic wake with vortex shedding keeping a symmetry plane and to the difference of the regime numbered II, with a zero mean lift. The different nature of the primary bifurcation completely modifies the transition scenario.

8.2.1. *Periodic vortex shedding with symmetry plane and zero mean lift (XIV)*

In the parameter subdomain touching the line corresponding to the rapid primary bifurcation of Hopf type, the real eigenvalue (or the slow complex eigenpair) no longer influences the wake dynamics. Because, in the asymptotic regime, both helical modes have the same amplitude the wake assumes a symmetry plane determined arbitrarily by initial conditions. The regular mode is absent; there is thus no mean shift of the wake off the flow axis as was the case in the regime II. The mean lift is therefore zero. Two examples of wake structure are given in figure 18. The found Strouhal number values are given in table 5. Overall, the Strouhal number varies only very weakly. It was close to 0.1 at both considered Prandtl numbers in the periodic regime with non-zero mean lift, and it is now close to 0.08 in the present case.

8.2.2. *Rotating vortex shedding with zero mean lift (XV) – $Pr = 0.72$*

At $Pr = 0.72$ a detailed scenario of transition from the periodic vortex shedding (XIV) to chaos is illustrated in figure 19, where the evolution of the lift path depending on Re is represented at $Ri = -0.2$ (see also the diagram in figure 4). At $Pr = 7$, the direct transition from the periodic vortex shedding to a rotating regime and a later onset of chaos was observed at $Ri = -0.5$. As the Reynolds number increases, the paths of the lift coefficient plotted in the (C_y, C_z) plane evolve from a slowly rotating regime with non-zero helicity representing the zero lift counterpart of regime (XIII) at $Re = 200$ to a path very slightly modulated by a secondary frequency at $Re = 210$. (The rotating ellipse is very flat and turns slowly so that the plot fills completely the central part of the figure.) The monoperiodic regime (apart from the period of the

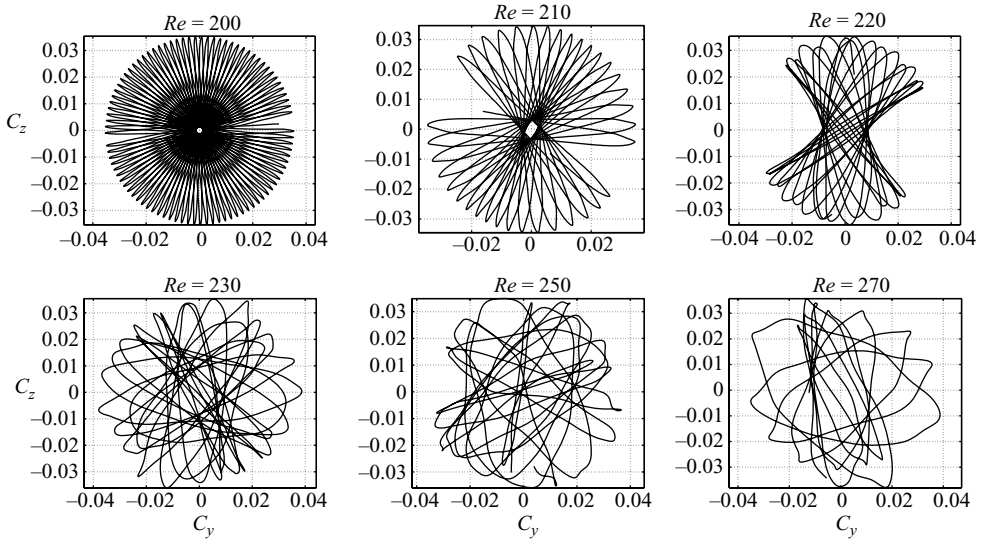

FIGURE 19. $Pr = 0.72$, $Ri = -0.2$: paths of lift coefficient in the plane normal to the flow axis for Reynolds number values indicated above the figures (regimes XV).

turning) is denoted by a filled square in figure 4. All other more or less modulated but still ordered regimes are marked as small filled squares inside larger square frames. In the next stage (third figure on the first line in figure 19) the ellipse, described at the basic Strouhal number of ~ 0.1, oscillates instead of turning in the same direction. At $Re = 230$ (first figure on the second line of figure 19), the rotation is back. The last two figures corresponding to $Re = 250$ and $Re = 270$ present a more entangled aspect. At first glance, there is no clear reason why one of them should be qualified as still ordered and the other one as chaotic.

To decide where to set the start of the chaotic regime we investigated the large time scales of the regimes. In figure 20, the first line of figures represents the 'time signals' of the y-axis projection of the lift coefficient (C_y), and the second line represents the corresponding Fourier transforms. The leftmost regime (at $Re = 200$) helps us to interpret the Fourier transform. The motion is governed by two principal frequencies, that of the oscillation along a single ellipse (corresponding to the highest peak of the Fourier transform, here almost exactly $St = 0.1$) and that of the ellipse rotation corresponding to about 500 non-dimensional time units, i.e. to $St = 0.002$ (corresponding to the distance of the peaks). At $Re = 250$ (middle column) the highest peak is situated at $St = 0.104$, and there is a great number of secondary peaks, the interval between which ($St \approx 0.006$) represents, again, the inverse of the period of rotation of the lift coefficient visible in the upper figure as an 'extinction' of the 'signal' corresponding to the instant at which the rotating ellipse (second to last one in figure 19) has a vertical orientation. (In the corresponding plot of figure 19 only one incomplete rotation period for $t > 900$ is represented.) There are two such 'extinctions' visible at e.g. $t \approx 730$ and $t \approx 900$ in the upper middle plot of figure 20. What changes considerably between $Re = 250$ and $Re = 270$ is the number of secondary peaks related to the 'signal' modulation. As long as all the secondary peaks are sharp and equally spaced we can consider the power spectrum to be characteristic of quasi-periodic, if not periodic, dynamics. At $Re = 270$ the low-frequency interval ($St < 0.05$) of the power spectrum is clearly no longer composed of discrete peaks. This can be

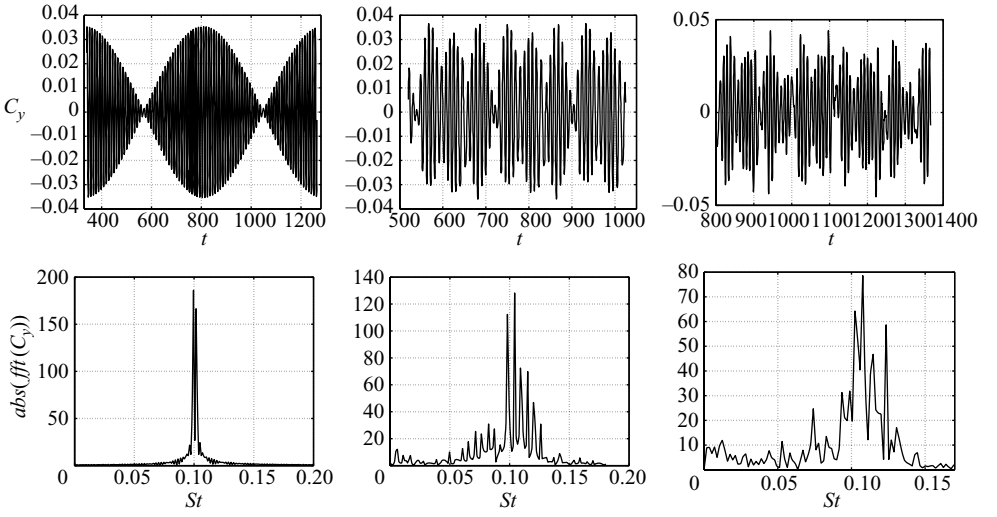

FIGURE 20. $Pr = 0.72$, $Ri = -0.2$: y-axis projection of the lift coefficient versus time at $Re = 200$, 250, 270 (upper figures from left to right) and the corresponding power spectra (absolute values of Fourier transforms).

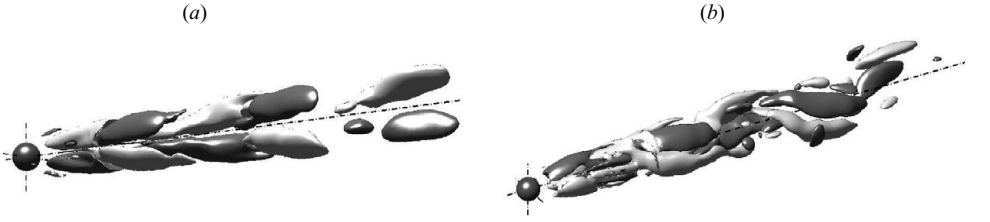

FIGURE 21. Wake structure at $Pr = 0.72$, $Ri = -0.2$ and (*a*) $Re = 200$, (*b*) $Re = 270$ represented in terms of isovorticity surfaces at $\omega_x = \pm 0.3$ in both cases.

explained by an absence of repetition of the patterns corresponding to one rotation with period $t \approx 170$ in the upper right of figure 20. It is seen that a clear proof of the chaotic nature of the regime is costly in terms of simulation time and that the onset of chaos is rather progressive. Nevertheless, with some error margin, chaos can be considered to occur between $Re = 250$ and $Re = 270$ at this Richardson and Prandtl numbers. The chaotic nature of the regime originates in the loss of periodicity on a very large time scale. Therefore there is nothing special that distinguishes the lift path at $Re = 270$ from that at $Re = 250$ (see the last figure in figure 19 corresponding to a trajectory in the interval $t \in [1250, 1330]$, i.e. for one rotation).

Represented in three dimensions, the flow pattern at $Re = 200$ is not distinguishable from that at $Re = 190$ corresponding to a periodic regime. This is easily understandable because the net helicity (measured by the aspect ratio of the rotating ellipse in the first plot of figure 19) is very small. The wake seems thus to keep its symmetry plane in figure 21(*a*). Nevertheless, a movie we set up from 200 snapshots over a rotation period is quite spectacular because it shows how the symmetry plane rotates. At $Re = 270$ (figure 21*b*) the helicity is already well developed, and there is no rest of planar symmetry visible. Small secondary structures start also to appear in the far wake in spite of a relatively high level of the vorticity set to represent them, $\omega_x = \pm 0.3$.

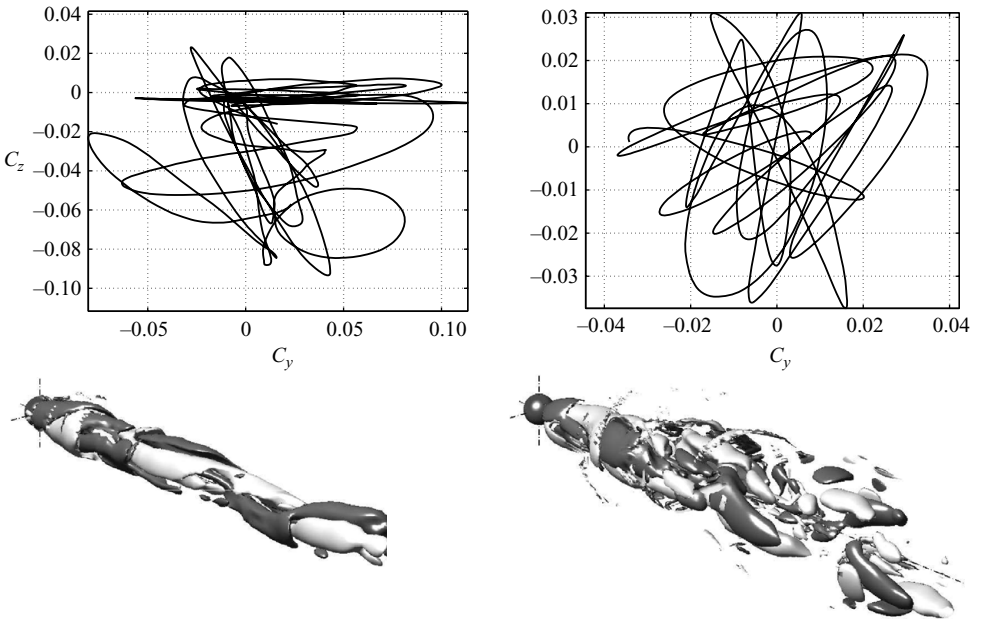

FIGURE 22. Lift paths (upper figures) and wake structure (lower figures) at $Pr = 0.72$. Left figures: $Ri = -0.03$ and $Re = 340$; right figures: $Ri = -0.2$, $Re = 300$. The level of axial vorticity surfaces is $\omega_x = \pm 0.1$ in the left figure and $\omega_x = \pm 0.3$ in the right figure. The mean lift is practically zero. (The ratio of the mean lift to r.m.s. of its fluctuations in the upper right plot is 1.6 %.)

To sum up, at higher Richardson numbers, the route to chaos starts from a periodic oscillating regime with zero mean lift and a symmetry plane. The latter gets lost due to a slow wake rotation. This rotation becomes more rapid, and a quasi-periodic modulation appears within it. Eventually, the dynamics end up losing any periodicity at very large time scales. At $Pr = 7$ we found a similar progression while sweeping along the $Ri = -0.5$ line. At both $Pr = 0.72$ and $Pr = 7$, a similar scenario was also found along the $Re = 100$ line by increasing the absolute value of the Richardson number from 0.25 to more than 1.

8.3. *Chaotic regimes (XII)*

In opposing flow chaos sets in much earlier than in assisting flow, therefore the flow pattern does not present so fine structures. Nevertheless, the flow is completely disordered. In figure 22 we present two examples of lift paths and wake structures at $Pr = 0.72$ at opposite ends of the investigated interval of Richardson numbers. In spite of the fact that the closest ordered regimes are qualitatively significantly different, the lift paths and the flow aspects are in all four cases similar: no symmetry left, (approximately) zero average lift, presence of helical structures. Only at the closest glance there subsists some fingerprint of the closest ordered regime. The almost horizontal oscillations of the lift coefficient at $Pr = 0.72$, $Ri = 0.03$ and $Re = 340$ (upper left of figure 22) are not due to a poorly converged simulation started from the closest regime with planar symmetry but due to an intermittent state reached after the lift coefficient described most of the chaotic entanglement visible in the plot.

8.4. *Intermediate transition zone*

Several interesting phenomena can be observed at the junction of the primary regular and Hopf bifurcation thresholds. At $Pr = 0.72$, it is interesting to note that the

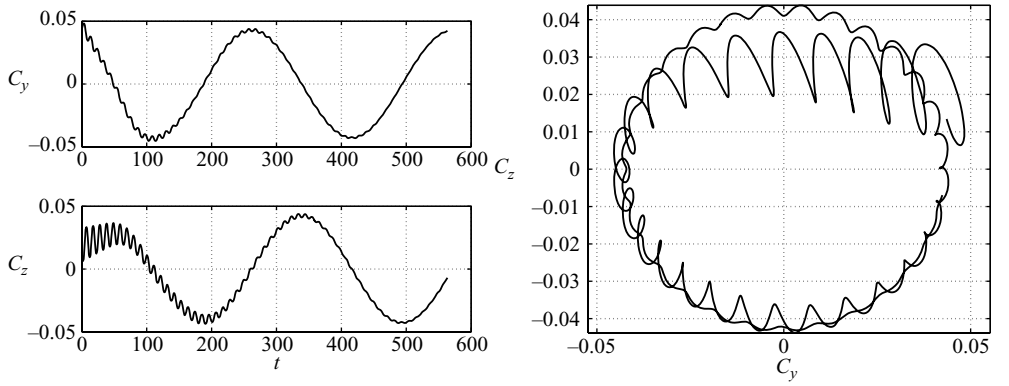

FIGURE 23. Simulation at $Pr = 7$, $Ri = -0.13$ and $Re = 180$ (XVI), starting from a slowly rotating, rapidly oscillating helical wake ($Ri = -0.13$, $Re = 190$).

vortex shedding with zero mean lift (XIV) penetrates rather deeply into the domain dominated otherwise by the regular bifurcation. Otherwise stated, if, at a Richardson number $Ri > -0.13$ (say at $Ri = -0.12$), the Reynolds number is increased from the regular-bifurcation threshold upward, the wake crosses the usual two early transition stages (steady non-axisymmetric wake (I) and periodic vortex shedding with non-zero mean lift (II)), but then the mean lift disappears, and the regime numbered XIV, characteristic of more negative Richardson numbers, sets in. The interpretation of this can be, in agreement with the observation made already for an unheated sphere ($Ri = 0$), that the coupling of the subspace associated with the real eigenvalue and that associated with the complex eigenpair tends to enhance the amplitude of the helical modes and reduce that of the steady one. For an unheated sphere ($Ri = 0$), this type of coupling explains why the secondary Hopf bifurcation sets in earlier than predicted by the linear analysis of the axisymmetric base flow. Close to the point at which the primary bifurcation type changes, the coupling ends up stabilizing the steady subspace, and only the oscillating modes subsist. The next stage, a quasi-periodic vortex shedding, is described below. It is found to exist at both investigated Prandtl numbers though not in the same Ri–Re domains.

At $Pr = 7$ the junction of the regular and the (rapid) Hopf bifurcations is marked by the presence of a new, slow Hopf bifurcation. As has been pointed out in § 4 the slow primary Hopf bifurcation represents the continuation of the regular one after collision of the two least stable real eigenvalues. The new complex eigenpair has very small imaginary parts corresponding to a Strouhal number of less than 0.003, i.e. to oscillations with a period exceeding 300 time units (see table 3). Although the pure slowly oscillating periodic regime associated with this eigenpair is stable only within a narrow zone along the primary-instability threshold it leaves a fingerprint in a much larger zone.

8.4.1. *Primary slow Hopf type regime (XVI) ($Pr = 7$)*

The proof of stability of this regime is provided in figure 23 at $Ri = -0.13$ and $Re = 180$. To investigate the character of the asymptotic state we ran two different simulations. One (represented in figure 23) corresponds to an initial condition taken from the closest slowly rotating, rapidly oscillating helical wake (regime XVII), and the other one was started from the closest wake with vortex shedding and planar symmetry (regime XIV). In both cases the rapid oscillation at $St \approx 0.1$ tends to disappear. In the

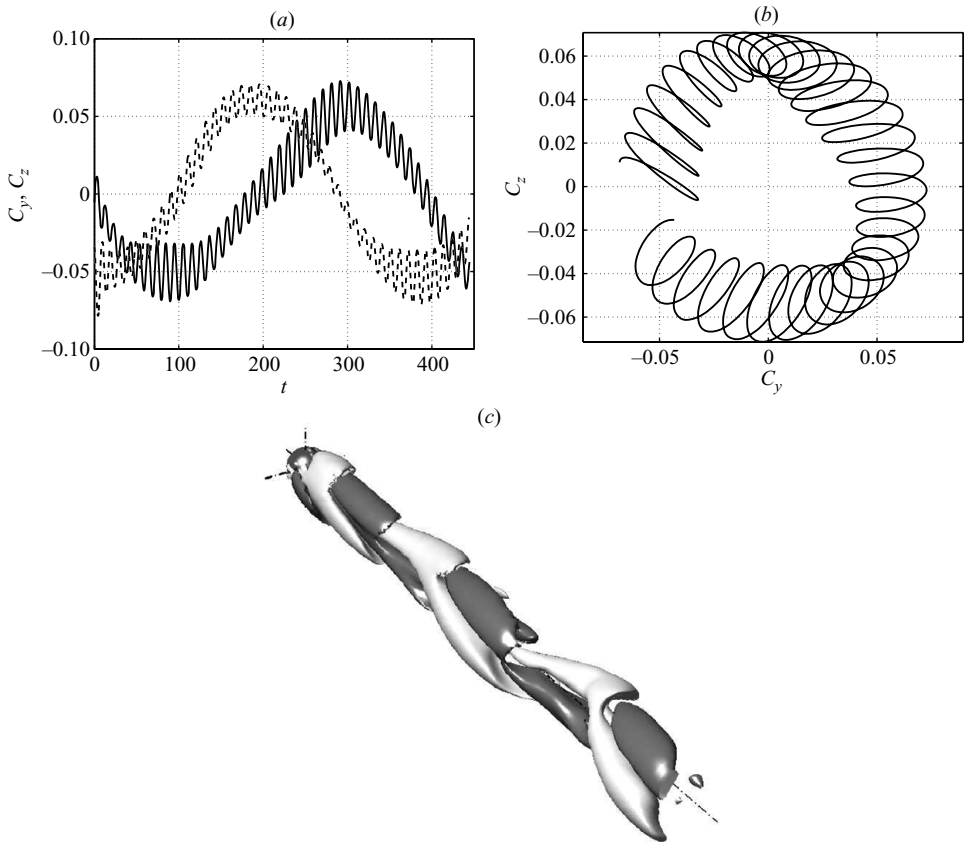

FIGURE 24. (*a*) Lift coefficient components C_y (full line) and C_z (dotted line) as functions of time at $Ri = -0.13$, $Re = 190$ and $Pr = 7$ (XVII). (*b*) Lift coefficient in the (C_y, C_z) plane at the same point of the parameter space. (*c*) Axial isovorticity surfaces at $\omega_x = \pm 0.1$ at $Re = 200$, $Ri = -0.13$ and $Pr = 7$.

first case, the lift slowly rotates about the flow axis, describing an almost perfect circle, which means that the solution contains only one helical mode associated with the (slow) unstable eigenpair. In the second case, the initial condition brings about, after a rapid decay of the rapidly oscillating mode, two slow helical modes with exactly the same amplitude, resulting in a very slow lift oscillation in a plane containing the flow axis. A weakly nonlinear theory allows only for one of the two states to be stable if nonlinear coupling of helical modes is present. Close to the threshold the couplings are very weak, and an extremely long simulation would have been necessary to let the unstable initial condition evolve to the stable asymptotic state. Nevertheless, the second simulation was found to present a rapid increase of the projection of the lift perpendicular to the initial symmetry plane, proving that the regime with two equal helical modes is unstable. Figure 23 thus represents the stable solution. Three-dimensional visualization of the vortical wake structure does not hold much interest because of the very slow rotation. The small helicity is not visible on the length scale of the computational domain extending only 25 diameters downstream of the sphere. At this scale, the axial vorticity isosurface is thus indistinguishable from that in regime I.

8.4.2. *Slowly rotating, rapidly oscillating helical wake (XVII) ($Pr = 7$)*

As seen by comparing figures 23 and 24, the regime results from a superimposition of two helical modes, one being slow and the other rapid. Note the $\pi/2$ phase shift

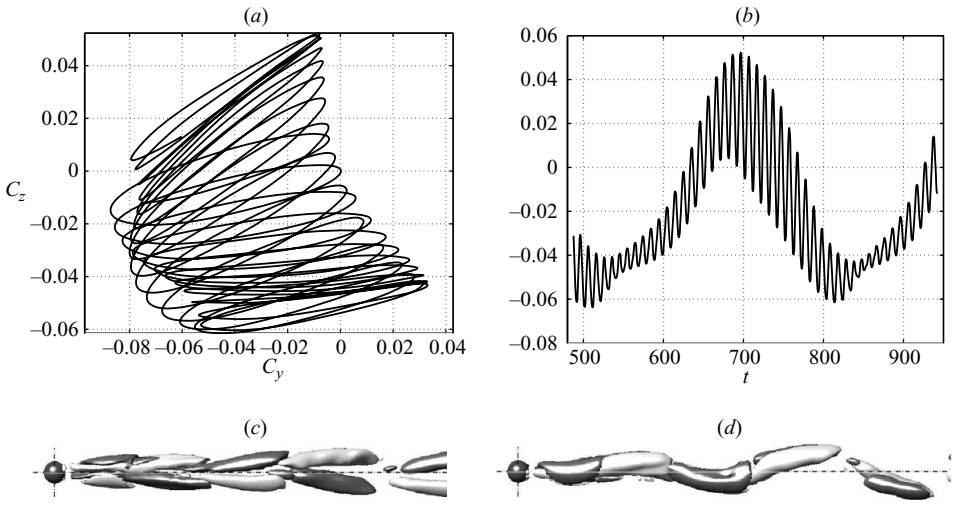

FIGURE 25. Simulation at $Pr = 7$, $Ri = -0.15$, $Re = 210$ (XVIII): (*a*) path of the lift coefficient in the (C_y, C_z) plane; (*b*) C_z versus time plot providing an idea of the period of the ellipse oscillation; (*c*), (*d*) two three-dimensional plots of the wake (surfaces at $\omega_x = \pm 0.2$) from two perpendicular views, showing a temporary symmetry.

of the slow oscillation yielding the almost perfectly circular motion due to the slow helical mode. Very soon (between $Re = 180$ and $Re = 185$ at $Ri = -0.13$), the rapid oscillations decaying in figure 23 become amplified and saturate to the new regime represented in figure 24. The latter is characterized by a superimposition of the slow helical mode, resulting from the slow primary eigenvalue, described in the previous section, and from a rapid helical one yielding the rapid spiral in figure 24(*b*). The Strouhal number of the rapid oscillations remains very close to $St = 0.1$; the slow rotation has a period of about 400 time units ($St = 0.0025$) in this case. The helical character of the rapid mode is clearly visible in figure 24(*c*). It is to be noted that, in spite of the qualitative resemblance of figures 17(*a*) and 24(*b*), the origin of regimes XIII and XVII is quite different. In regime XIII the slow rotation is due to the coupling between a steady and an oscillating state. A closer look at the flow structure (figures 17*c* and 24*c*) shows also that the wake in regime XIII is very close to having a planar symmetry while that in regime XVII is clearly helical.

8.4.3. *Slowly laterally oscillating helical wake (XVIII) ($Pr = 7$)*

This regime assures the transition between regimes with planar symmetry and zero mean lift on the side of more negative Richardson numbers and those with a non-zero mean lift on the side of less negative Richardson numbers. In the (C_y, C_z) plane, it is characterized by an ellipse, described with the typical rapid Strouhal number close to 0.1 that changes periodically both its aspect ratio and its direction. The direction of the ellipse no longer rotates; it oscillates within a certain angle. There is no permanent planar symmetry, but at the moment at which the ellipse is flat the wake assumes temporarily a symmetrical aspect.

The slow frequency evolves from a value obviously linked to the slow eigenpair responsible for the two previously described regimes (XVI, XVII) in the regime represented in figure 25 to a Strouhal number of about 0.01, i.e. to a period about three times shorter, in figure 26(*d*). In figure 25(*c*, *d*) the temporary symmetry plane has been captured. The lift paths are represented over one (long) oscillation period of

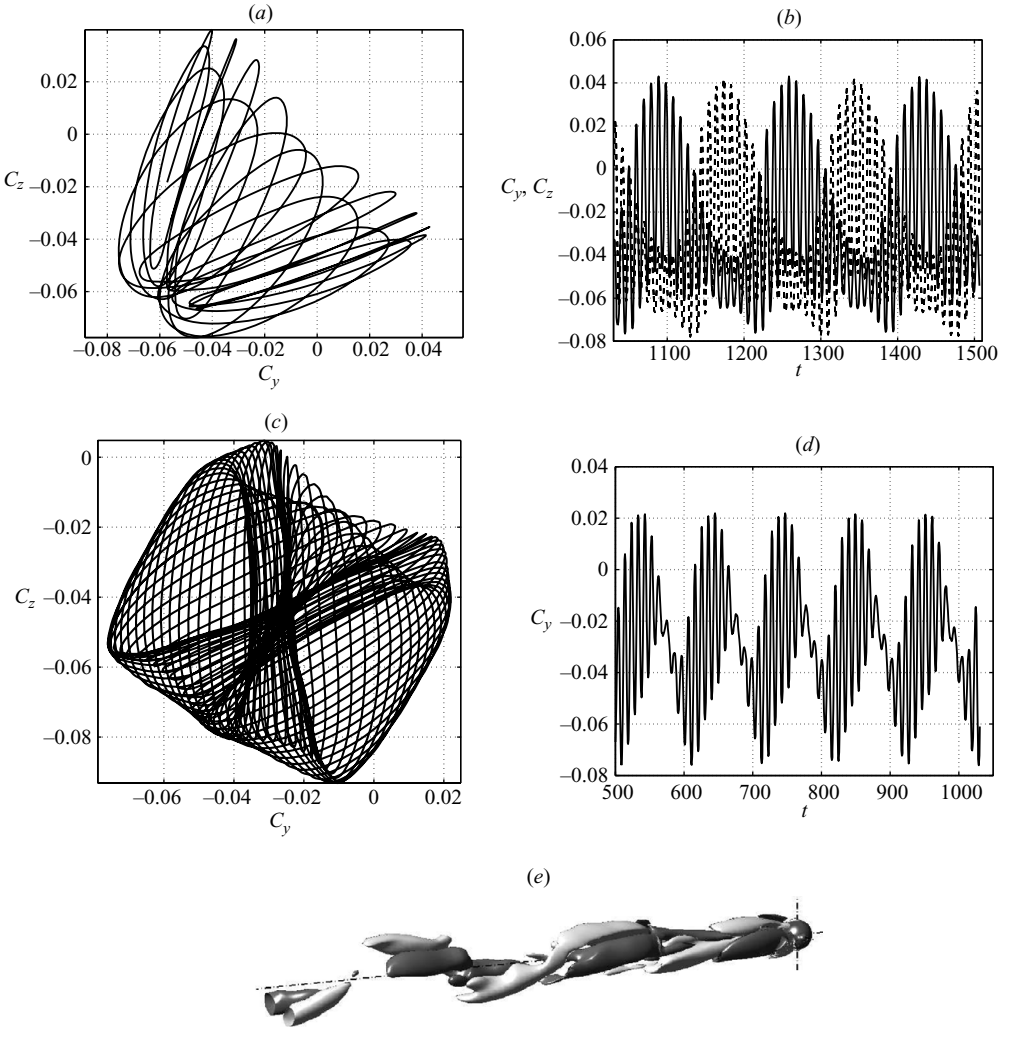

FIGURE 26. (*a*), (*b*) Path of the lift coefficient and C_y, C_z versus time plot (full line: C_y; dashed line C_z) at $Pr = 7$, $Ri = -0.15$ and $Re = 220$. (*c*), (*d*), (*e*) $Pr = 7$, $Ri = -0.13$ and $Re = 240$. (*c*) Path of the lift coefficient; (*d*) C_y versus time plot; (*e*) wake structure ($\omega_x = \pm 0.2$). Both cases are examples of regimes numbered XVIII.

the ellipse except for figure 26(*c*), where five periods of about 100 time units each are plotted to show the regular biperiodic dynamics resembling a Lissajous figure. At the upper and left limits, the subdomain is bordered by rotating regimes presenting one more frequency, intermediate between the slow rotation and rapid oscillation. This results in a seemingly chaotic lift path (see figure 27*a*). Nevertheless, the C_y versus time plots (figure 27*b*) still present an obvious periodicity on the scale of a 100 time units. The new frequency is clearly comparable to the quasi-periodic modulation of the regimes III and XX (see § 8.4.5).

8.4.4. *Slowly laterally oscillating helical wake (XIX) ($Pr = 0.72$)*

At $Pr = 0.72$ a similar behaviour was found in a very restricted parameter domain, namely at $Ri = -0.1$ and $Re = 230, 240$ (figure 28). The regime is characterized by

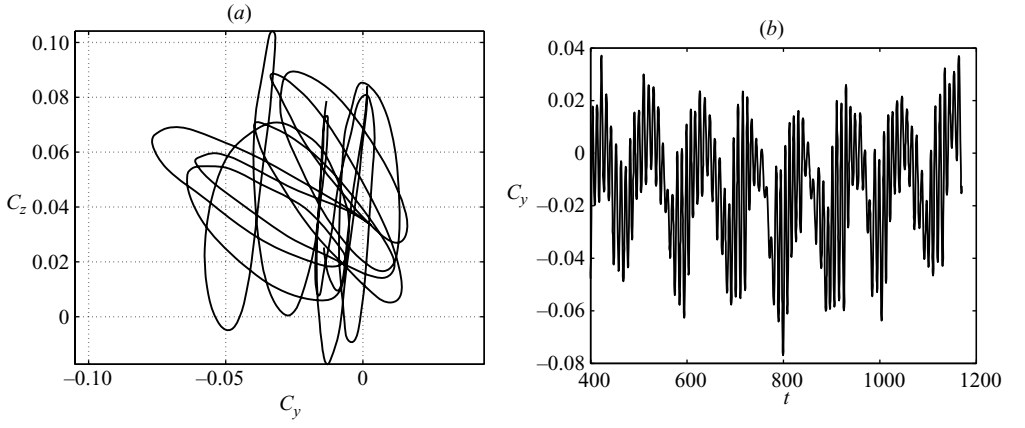

FIGURE 27. (*a*) Path of the lift coefficient and (*b*) C_y versus time plot at $Pr = 7$, $Ri = -0.1$ and $Re = 270$ (XVIII).

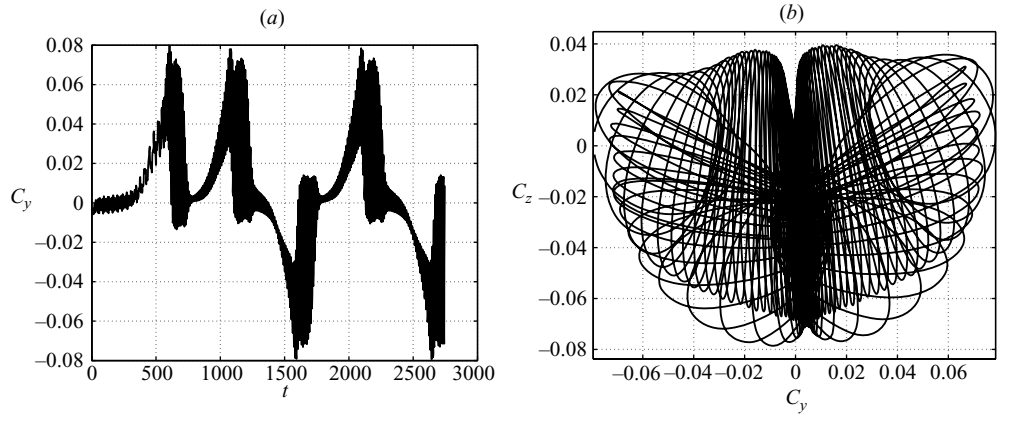

FIGURE 28. Simulation at $Pr = 0.72$, $Ri = -0.1$ and $Re = 230$ (XIX): (*a*) C_y versus time; (*b*) lift path over the last 1100 time units (period) of (*a*).

oscillations with varying helicity and varying principal oscillation direction. The found dynamic has an extremely large period of about 1100 time units at $Re = 230$ due to the toggling of the predominant lift direction from $C_y > 0$ to $C_y < 0$. It presents, again, a temporary symmetry plane. At $Re = 240$ the toggling is absent, yielding a period of about 550 time units.

8.4.5. *Quasi-periodic vortex shedding with planar symmetry and zero mean lift (XX)*

At $Pr = 0.72$ this regime was found to exist only in the intermediate zone at Richardson numbers between -0.09 and -0.17, whereas at $Pr = 7$, it is situated more to the left, between $Ri = -0.17$ and $Ri = -0.4$. It is the counterpart of the quasi-periodic regime III except for the mean lift, which is zero in the present case. The basic difference between this regime and the quasi-periodic regime III described in § 6.3 is analogous to that between figures 7 and 18. The wake presents a symmetry plane and oscillates symmetrically about the flow axis, and the oscillations have quasi-periodic dynamics with (at least) two frequencies. The fast frequency is approximately that

of the periodic regime ($St \approx 0.1$). The time dependence of the lift coefficient (and all other flow variables) is mainly governed by this frequency and a secondary one corresponding to $St \approx 0.03$.

9. Global characteristics: drag and lift coefficients, Nusselt number

In an unheated sphere wake the drag coefficient is only weakly affected by instabilities (see Bouchet *et al.* 2006). It is so because it is related only to the $m = 0$ mode, which is modified by the primary instability only proportional to the square of the instability amplitude. The Nusselt number integrates the heat flux over the whole sphere surface and is thus also related to the $m = 0$ mode. In contrast, the modification of the lift is a first-order effect and is expected to be affected by the changes of regimes in a non-negligible way. The same is to be expected in mixed convection. Because of the different scales of the plots, the results are presented separately for assisting and opposing flows.

Whenever the flow regimes are unsteady, the values of drag coefficient and Nusselt number are taken as time averages. The root mean square (r.m.s.) of the drag and heat flux fluctuations in all our simulations was found to be less than 1 % of the mean values in all unsteady regimes, even in chaotic ones. Therefore we present r.m.s. of fluctuations only for lifts in unsteady regimes. The symbols on the curves represent points at which the value was computed and correspond to concrete flow regimes as defined in the legend of figures 2 and 4.

9.1. *Assisting flow*

The drag coefficients as functions of Reynolds number ($0 \leqslant Re \leqslant 1000$) for different values of Grashof number ($0 \leqslant Gr \leqslant 5 \times 10^5$) at $Pr = 0.72$, obtained from axisymmetric simulations, were plotted in figure 7 in Kotouč *et al.* (2008). The available bibliography provides mostly data at low Reynolds numbers lying perfectly in the axisymmetric domain. In Kotouč *et al.* (2008) it was shown that our axisymmetric simulations reproduce very well e.g. the relations proposed by Hieber & Gebhart (1969). Although it was shown, in the same paper, that most of the obtained values are physically relevant, some of them lay beyond the regular-instability threshold. The main question that arises is how the different three-dimensional regimes modify the mean value and the amplitude of the drag coefficient.

Figure 29 shows the curves of the drag coefficient as a function of Re at both $Pr = 0.72$ and $Pr = 7$ and at several Ri numbers. In unsteady regimes, mean values are plotted. No change in the slope of the curves when passing either from axisymmetric to three-dimensional flows or through different three-dimensional regimes is visible. Bouchet *et al.* (2006) reported a change in the slope of the curves at each bifurcation; the observed change of the slopes is, however, too small to be distinguished in the curves of figure 29. However, if the drag of axisymmetric flow is compared to the correct curve obtained in a fully three-dimensional simulation, there is a clear difference: the instability shifts the drag upward (see inset in figure 29). The r.m.s. of the drag oscillations in our simulations was found to be less than 1 % of the mean value in all unsteady regimes. Therefore it was not plotted.

One of the most visible effects of the three-dimensionality of the flow is the existence of a lift. In figure 30 we present the mean values of the instantaneous lift coefficients, defined as

$$C_L = \sqrt{<C_y>^2 + <C_z>^2}, \tag{9.1}$$

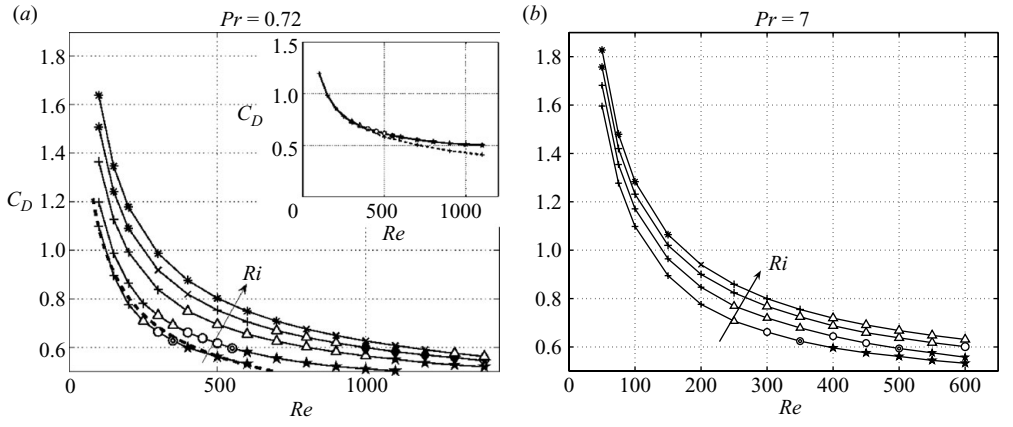

FIGURE 29. Values of the drag coefficient as a function of Re (a) at $Ri = 0$, 0.1, 0.3, 0.5 and 0.7 at $Pr = 0.72$ and (b) at $Ri = 0$, 0.1, 0.2 and 0.3 at $Pr = 7$. The different symbols, used also in figures 30–32, represent points at which the values of the drag coefficient were computed and correspond to the flow regimes defined in the legend of figure 2. The values of the drag coefficient are connected by straight lines to help to associate points corresponding to a constant Richardson number. Dashed line: empirical law of Clift, Grace & Weber (1978) for unheated sphere ($Ri = 0$). Inset: comparison of the real drag (full line) and the result of axisymmetric computation at $Ri = 0.1$ (dashed line).

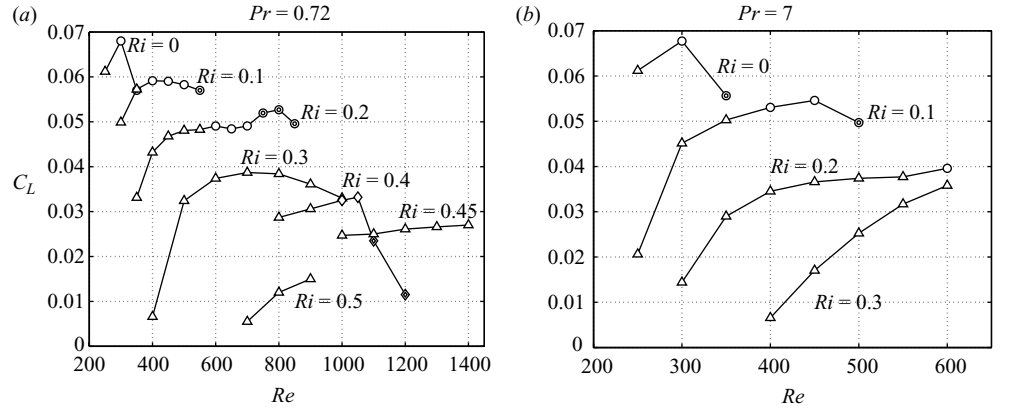

FIGURE 30. Mean value of the lift coefficient as a function of Re for a few selected values of Ri at (a) $Pr = 0.72$ and (b) $Pr = 7$, connected by straight lines.

where $<C_y>$ and $<C_z>$ are the time averages of the projections of lift coefficient onto y- and z-axis perpendicular to the flow direction as a function of Re for all values of Ri. Only cases in which such a value is meaningful are considered. The mean lift of chaotic regimes (XII), as well as that of the non-periodic rotating regimes (XI), where the symmetry plane has already been broken, are considered zero and thus are not plotted in the figure. The typical path of the projection of the lift coefficient onto a plane perpendicular to the flow axis, shown in figure 16(a), allows to conclude that even if at short time scales the average seems to be non-zero, its long-time-converged value is zero. Note also that the lift is zero for steady regimes with four (IV) and six (V) vorticity threads and that its average value is zero for the planar symmetric periodic regime with four oscillating vorticity threads (VII). In contrast with the drag

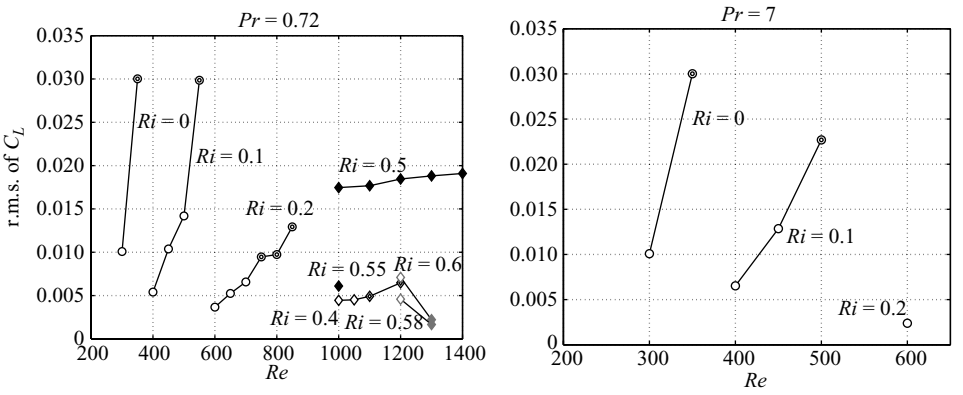

FIGURE 31. The values of r.m.s. of the lift coefficients.

coefficient, the lift coefficient presents significant changes of trend at each change of regime. In spite of the different shape of each plotted curve (corresponding to a constant Ri), which is due to the fingerprint of the rich variety of flow regimes evidenced, the trend of the lift is to decrease with increasing Richardson number.

The description of the lift forces in different unsteady regimes would be incomplete if a value, describing the amplitude of the oscillations, were not supplied. The r.m.s., defined as

$$r.m.s.\,(C_L) = \sqrt{\langle (C_y - <C_y>)^2 \rangle + \langle (C_z - <C_z>)^2 \rangle}, \tag{9.2}$$

(<> stands, again, for a time average) is plotted for all, except chaotic (XII) and nonplanar-symmetric (XI) regimes in figure 31. The latter were not included in the plot because the simulations could not be run systematically until convergence. (Note that the r.m.s. is used to accommodate all the non-periodic regimes in their variety and not because of a statistical sampling.)

Again, a global trend is towards growing fluctuations of the wake with Re for a constant Ri. A change in the slope of those curves is visible when a sub-harmonic frequency sets in – the fluctuations are enhanced. In contrast, the wake fluctuations are attenuated as Ri grows.

The overall Nusselt number, defined as

$$Nu = 2\frac{\dot{Q}}{\dot{Q}_{cond,th}}, \tag{9.3}$$

where

$$\dot{Q}_{cond,th} = 2\pi\lambda(T_S - T_\infty)d \tag{9.4}$$

is the theoretical, purely conductive heat flux and $\dot{Q}$ is a calculated overall (conductive and advective) heat flux, is plotted as a function of Reynolds number for different constant values of Richardson number in figure 32 for both (a) $Pr = 0.72$ and (b) $Pr = 7$. Similarly to the drag coefficient plots, no visible change in the slopes of curves related to the changes of regimes were observed at $Pr = 0.72$. The Nusselt number, Nu, increases with Re for a constant Ri and increases with Ri for a constant Re. Therefore the curves do not cross each other. Figure 32(a) contains also the experimental law of Yuge (1960; dashed line), and the inset provides comparison between axisymmetric computation at $Ri = 0.1$ and numerical results

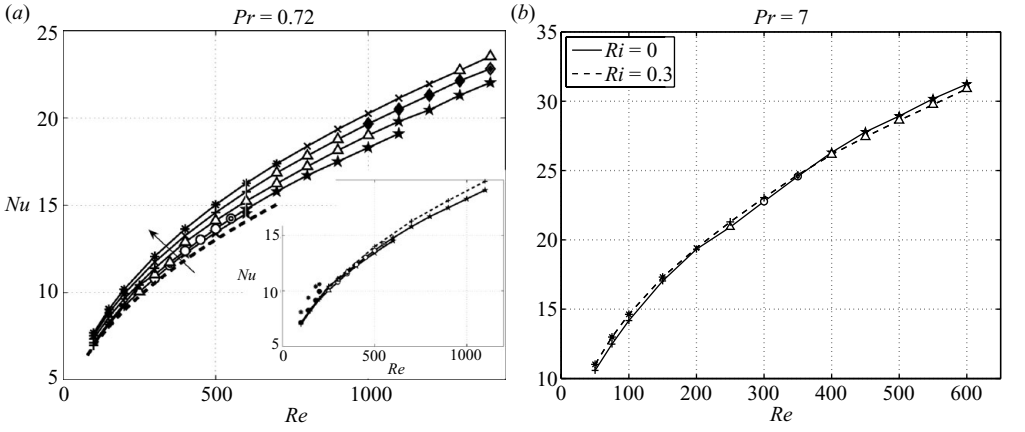

FIGURE 32. The (average, in unsteady regimes) Nusselt number as a function of Re for $Ri = 0,\ 0.1,\ 0.2,\ 0.3$ and 0.5 at (a) $Pr = 0.72$ and for $Ri = 0$ and 0.3 at (b) $Pr = 7$, connected by straight lines. (a) Dashed line: empirical law of Yuge (1960) at $Ri = 0$ – for higher Ri the law does not apply to Reynolds number exceeding 100; inset: comparison to axisymmetric computation (dashed line) at $Ri = 0.1$; bullets and asterisks between $Re = 100$ and 200: results of Bhattacharyya & Singh (2008) at $Ri = 0$ and 0.1, respectively; short full line: $Ri = 0$; long full line: $Ri = 0.1$.

of Bhattacharyya & Singh 2008. Yuge's (1960) law seems to underestimate and Bhattacharyya & Singh 2008 seem to overestimate the Nusselt number.

In contrast, as shown in Kotouč *et al.* (2008), the value of the Nusselt number at $Pr = 7$ is more sensitive to the different types of flow regimes. As a result, before the onset of recirculation, the curves Nu versus Re depend on Ri, whereas beyond the recirculation threshold they would be practically superimposed if three-dimensionality did not set in. For clarity, the Nusselt number dependence on the Reynolds number was plotted only for the extreme values of Ri (0 and 0.3) in figure 32(b). It is seen that the dashed line of $Ri = 0.3$ approaches the solid line of $Ri = 0$ at $Re = 200$. Without the transition to three-dimensionality of the $Ri = 0$ flow both curves would cross at $Re = 250$, the threshold of the onset of recirculation for $Ri = 0.3$. Instead the primary bifurcation lowers the Nusselt number and shifts the solid curve downward. The consecutive regimes reverse the trend and increase the slope. Finally, at $Re \approx 370$ the curves cross when the three-dimensional regime sets in at $Ri = 0.3$.

9.2. *Opposing flow*

Figure 33 shows, again, the dependence of the drag coefficient on Reynolds number for a few selected Richardson numbers. In opposing flow, contrarily to the trend in the assisting flow configuration, the drag coefficient decreases for increasing absolute value of Richardson number at constant Reynolds number. This is clearly due to the buoyant forces near the sphere surface and their opposing effect on the inertial forces resulting in a reduced pressure gradient. The decrease of drag with decreasing Ri at a constant Re is somewhat stronger at $Pr = 0.72$. The curves at $Ri = 0$ are, of course, identical for both Prandtl numbers because, in this case, the velocity field is uncoupled from the temperature one. They are, of course, also identical to that represented in § 9.1 concerning assisting flow. The change in the slope of the $Ri =$ constant curves is almost invisible at the regular bifurcation. The Hopf bifurcation enhances the drag coefficient. This enhancement is stronger when the Hopf bifurcation appears in the steady axisymmetric flow (as a primary bifurcation) at more negative Richardson

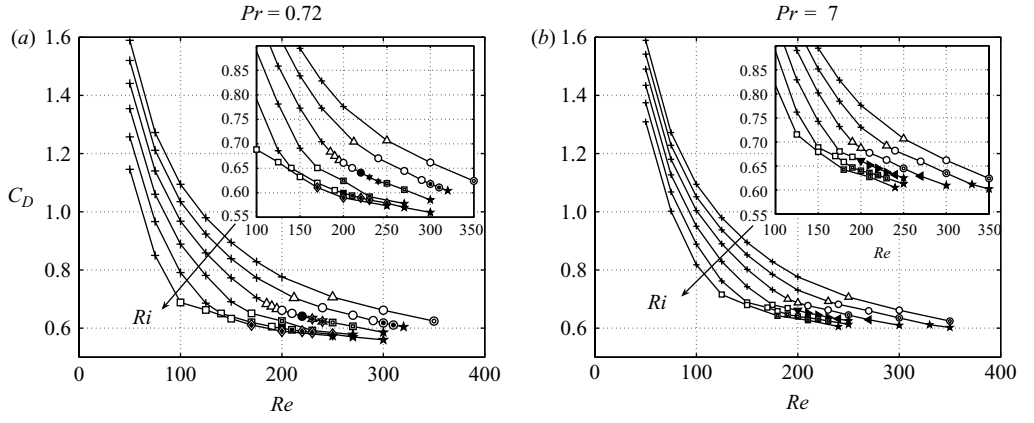

FIGURE 33. The drag coefficient as a function of Re for (a) $Pr = 0.72$ and (b) $Pr = 7$ with detailed views in the upper right corners at $Ri = 0, -0.05, -0.1, -0.15, -0.2$ and -0.25. The arrows indicate an increase of the absolute value of Ri.

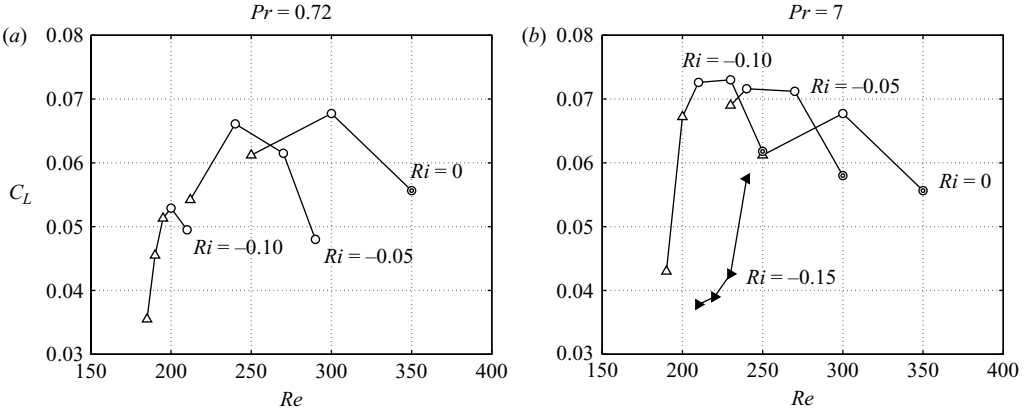

FIGURE 34. The mean lift coefficient as a function of Re for (a) $Pr = 0.72$ and (b) $Pr = 7$ for a few selected values of Ri.

numbers. At the secondary Hopf bifurcation, the change of the trend of the curves is weak again. The changes of slope of the curves for $Ri \leqslant -0.1$ are better visible in the detailed views in the upper right corners of figure 33.

Figure 34 shows the values of the lift coefficient as functions of Re for some selected Ri. In unsteady regime the time-averaged lift coefficient is represented. Note that the mean value of the lift of oscillatory regimes with planar symmetry XIV and XX is zero. In the same way, the mean lifts of chaotic regimes XII, as well as that of all rotating regimes, are considered zero and thus are not plotted in the figure. Roughly speaking, the mean lift coefficient decreases with increasing $|Ri|$ at $Pr = 0.72$, whereas it increases at $Pr = 7$ between $Ri = 0$ and $Ri = -0.1$. The onset of oscillations tends to make the mean lift decrease. The maxima of the plotted curves are always reached shortly after the onset of the secondary Hopf bifurcation.

The values of the r.m.s. of the fluctuations of lift coefficient are plotted in figure 35. The trend towards increasing amplitudes with increasing Re for a constant Ri appeares to be limited to the earliest stages of transition at both values of Pr.

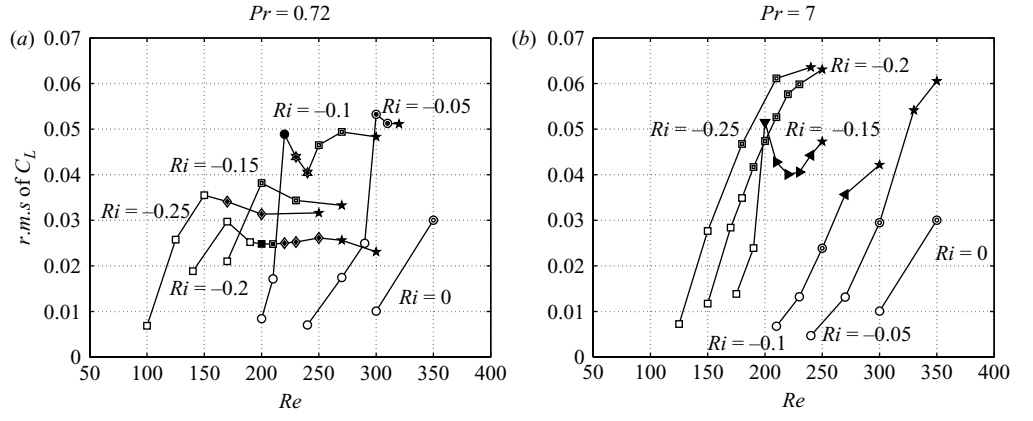

FIGURE 35. The r.m.s. values of the lift coefficient as a function of Re for (a) $Pr = 0.72$ and (b) $Pr = 7$ for a few selected Ri.

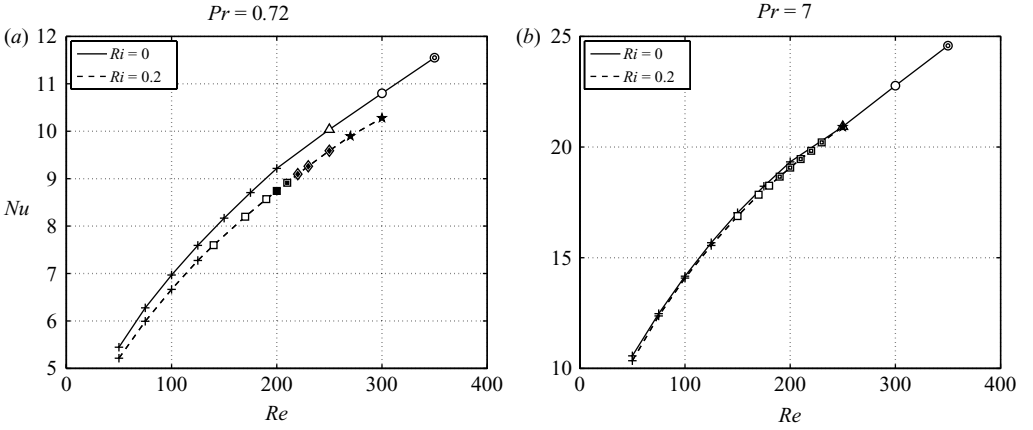

FIGURE 36. The Nusselt number as a function of Re for (a) $Pr = 0.72$ and (b) $Pr = 7$ for two extreme values of Ri: $Ri = 0$ and $Ri = -0.2$.

Figure 36 shows the values of the Nusselt number. The dependence of Nu on Re was plotted only for two extreme cases: $Ri = 0$ and $Ri = -0.2$. At $Ri = 0$, where at both Prandtl numbers the flow regimes are the same, the Nusselt number at $Pr = 7$ is approximately twice as high as that at $Pr = 0.72$. This is due to a reduced diffusive heat transfer at higher Prandtl numbers (the dependence of Nu on Pr was shown in Kotouč *et al.* 2008). In the same paper, it was shown that, at $Pr = 0.72$, the sensitivity of Nu to the Richardson number Ri at a constant Re is stronger. This can be clearly seen in figure 36 – the gap between the curves of $Ri = 0$ and $Ri = -0.2$ for a constant Re is much greater at $Pr = 0.72$ than at $Pr = 7$. In both cases, Nu decreases as the absolute value of Ri increases for a constant Re. This, again, is due to the adverse action of the buoyant forces, which thicken the thermal and velocity boundary layers. The change in the slope of the Nu versus Re dependence (mainly visible at $Pr = 7$) is due to supercritical regimes. It has already been evidenced in assisting flow. It lowers the slope of the curves at the onset of three-dimensionality. Roughly speaking, the transition affects the Nusselt number only weakly.

10. Conclusions

In this paper, investigations of three-dimensional steady and unsteady flow regimes of a flow past a fixed heated sphere in mixed convection in the configurations of assisting and opposing flows have been carried out. The three-dimensional Ri–Re–Pr parameter space was swept for two fixed values of Prandtl number (0.72 and 7) in a domain corresponding to transition from a steady axisymmetric flow to chaos.

Despite the stabilizing effect of assisting flow, at least up to $Ri \approx 1$ the flow appears to loose its linear stability. The most striking feature of the transition in assisting flow is the important role of higher azimuthal subspaces $m > 1$. The first stage of transition consists, in all the investigated cases of assisting flow, in axisymmetry breaking via a regular bifurcation, but the bifurcation arises in azimuthal subspaces characterized by increasing azimuthal wavenumbers when the Richardson number grows. The scenario typical for an unheated sphere is limited to Richardson numbers smaller than 0.3 both for the low (0.72) and high (7) Prandtl numbers considered here. At higher Richardson numbers completely new transitional regimes arise as a result of coupling of two or more azimuthal subspaces.

In opposing flow, the destabilizing effect of the convection shifts the primary-instability threshold to lower Reynolds numbers. The transition represents a continuation of the trend observed in assisting flow only in a very restricted domain of small negative Richardson numbers ($Ri > -0.1$). Its main feature is the presence of a primary Hopf bifurcation at more negative Richardson numbers. The lines representing the threshold of the primary regular and Hopf bifurcations intersect at $Ri = -0.13$ for $Pr = 0.72$. At Richardson numbers close to this intersection the transition scenario is characterized by clearly identified nonlinear states related to both types of bifurcations. At $Pr = 7$ a still more intriguing phenomenon has been evidenced. Before intersecting the threshold of the rapid Hopf bifurcation, the regular bifurcation gives way to a slow Hopf bifurcation arising due to a collision of two real eigenvalues giving rise to a complex eigenpair with a small imaginary part. The fingerprint of this slow eigenpair is characteristic of the transitional regimes in a whole domain between $Ri = -0.1$ and $Ri = -0.2$ at $Pr = 7$. At more negative Richardson numbers the scenario is qualitatively similar for both investigated Prandtl numbers. It consists of a primary regime with vortex shedding, zero mean lift and a symmetry plane related directly to the Hopf bifurcation. This symmetry gets lost rather rapidly due to the onset of rotation of the symmetry plane around the flow axis in a relatively long stage of transition to chaotic dynamics.

The combined results obtained for assisting and opposing flows show that convective effects yield a very large variety of regimes that must be taken into account especially if more refined information is needed than just the drag and the global Nusselt number. The transitional regimes are likely to have an especially significant impact on sedimentation of millimetric particles in water and sub-millimetric ($d \sim 0.1$ mm) particles in air and are likely to be still more important for the dynamics of rising (light) particles. Beyond this application, the evidenced transition scenarios represent an interesting theoretical laboratory shedding light on the large variety of possible nonlinear phenomena.

The presented study allows us also to assess the strength and the limits of the methodology of parametric investigation. The advantage of such investigations consists in providing a comprehensive overview covering, in principle, any particular configuration. However, the number of parameters rapidly grows proportional to the complexity of phenomena accounted for. The next logical stage is, for example, the investigation of freely moving spheres with an account of thermal effects. This adds

another parameter (solid/fluid density ratio) to the problem description. Despite the fact that, technically, the problem of simulation of the free sphere motion has already been solved in a sufficiently efficient way to enable a parametric investigation, the question of feasibility and relevance of such a study has to be raised, in particular, in view of serious limitations of the Boussinesq model.

REFERENCES

Ayyaswamy, P. S. 1999 *Combustion Dynamics of Moving Droplets*, vol. 1. Gulf Publishing.

Bar-Ziv, E., Zhao, B., Mograbi, E., Katoshevski, D. & Ziskind, G. 2002 Experimental validation of the Stokes law at nonisothermal conditions. *Phys. Fluids* **14**, 2015–2018.

Bhattacharyya, S. & Singh, A. 2008 Mixed convection from an isolated spherical particle. *Intl J. Heat Mass Transfer* **51**, 1034–1048.

Bouchet, G., Mebarek, M. & Dušek, J. 2006 Hydrodynamic forces acting on a rigid fixed sphere in early transitional regimes. *Euro. J. Mech.* **25**, 321–336.

Chen, T. S. & Mucoglu, A. 1977 Analysis of mixed forced and free convection about a sphere. *Intl J. Heat Mass Transfer* **20**, 867–875.

Chiang, C. H. & Sirignano, W. A. 1993 Interacting, convecting, vaporizing fuel droplets with variable properties. *Intl J. Heat Mass Transfer* **36**, 875–886.

Clift, R., Grace, J. R. & Weber, M. E. 1978 *Bubbles, Drops and Particles*. Academic.

Danaila, I., Dušek, J. & Anselmet, F. 1998 Nonlinear dynamics at a Hopf bifurcation with axisymmetry breaking in a jet. *Phys. Rev.* E **57**, 3695–3698.

Dudek, D. R., Fletcher, T. H., Longwell, J. P. & Sarofim, A. F. 1988 Natural convection induced drag forces on spheres at low Grashof numbers: comparison of theory with experiment. *IntL J. Heat Mass Transfer* **31**, 863–873.

Gan, H., Chang, J., Feng, J. J. & Hu, H. H. 2003 Direct numerical simulation of the sedimentation of solid particles with thermal convection. *J. Fluid Mech.* **481**, 385–411.

Geoola, F. & Cornish, A. R. H. 1982 Numerical simulation of free convective heat transfer from a sphere. *IntL J. Heat Mass Transfer* **25**, 1677–1687.

Ghidersa, B. & Dušek, J. 2000 Breaking of axisymetry and onset of unsteadiness in the wake of a sphere. *J. Fluid Mech.* **423**, 33–69.

Hieber, C. A. & Gebhart, B. 1969 Mixed convection from a sphere at small Reynolds and Grashof numbers. *J. Fluid Mech.* **38**, 137–159.

Jenny, M. & Dušek, J. 2004 Efficient numerical method for the direct numerical simulation of the flow past a single light moving spherical body in transitional regimes. *J. Comput. Phys.* **194**, 215–232.

Jenny, M., Dušek, J. & Bouchet, G. 2004 Instabilities and transition of a sphere falling or ascending freely in a Newtonian fluid. *J. Fluid Mech.* **508**, 201–239.

Jeong, J. & Hussain, F. 1995 On the identification of a vortex. *J. Fluid Mech.* **285**, 69–94.

Jia, H. & Gogos, G. 1996 Laminar natural convection heat transfer from isothermal spheres. *Intl J. Heat Mass Transfer* **39**, 1603–1615.

Johnson, T. A. & Patel, V. C. 1999 Flow past a sphere up to a Reynolds number of 300. *J. Fluid Mech.* **378**, 19–70.

Katoshevski, D., Zhao, B., Ziskind, G. & Bar-Ziv, E. 2001 Experimental study of the drag force acting on a heated particle. *J. Aerosol Sci.* **32**, 73–86.

Klyachko, L. S. 1963 Heat transfer between a gas and a spherical surface with the combined action of free and forced convection. *J. Heat Transfer* **85**, 355–357.

Kotouč, M. 2008 Transition à la turbulence du sillage d'une sphre fiwe ou libre en convection mixte. PhD thesis, Université Louis Pasteur, Strasbourg I.

Kotouč, M., Bouchet, G. & Dušek, J. 2008 Loss of axisymmetry in flow past a heated sphere - assisting flow. *Intl J. Heat Mass Transfer* **51**, 2686–2700.

Lecordier, J. C., Hamma, L. & Paranthoen, P. 1991 The control of vortex shedding behind heated circular cylinders at low Reynolds numbers. *Exp. Fluids* **10**, 224–229.

McLeod, P., Riley, D. S. & Sparks, R. S. J. 1996 Melting of a sphere in hot fluid. *J. Fluid Mech.* **327**, 393–409.

Michalke, A. 1984 Survey on jet instability theory. *Prog. Aerospace Sci.* **21**, 159–199.

Mittal, R. 1999 A Fourier--Chebyshev spectral collocation method for simulating flow past spheres and spheroids. *Intl J. Numer. Meth. Fluids* **30**, 921–937.

Mograbi, E. & Bar-Ziv, E. 2005*a* Dynamics of a spherical particle in mixed convection flow field. *J. Aerosol Sci.* **36**, 387–409.

Mograbi, E. & Bar-Ziv, E. 2005*b* On the mixed convection hydrodynamic force on a sphere. *J. Aerosol Sci.* **36**, 1177–1181.

Mograbi, E., Ziskind, G., Katoshevski, D. & Bar-Ziv, E. 2002 Experimental study of the forces associated with mixed convection from a heated sphere at small Reynolds and Grashof numbers. Part II. Assisting and opposing flows. *Intl J. Heat Mass Transfer* **45**, 2423–2430.

Mucoglu, A. & Chen, T. S. 1978 Mixed convection about a sphere with uniform surface heat flux. *J. Heat Transfer* **100**, 542–544.

Najjar, F. M. & Balachandar, S. 1996 Low-frequency unsteadiness in the wake of a normal flat plate. *J. Fluid Mech.* **370**, 101–147.

Natarajan, R. & Acrivos, A. 1993 The instability of the steady flow past spheres and disks. *J. Fluid Mech.* **254**, 323–344.

Nguyen, H. D., Paik, S. & Chung, J. N. 1993 Unsteady mixed convection heat transfer from a solid sphere: the conjugate problem. *Intl J. Heat Mass Transfer* **36**, 4443–4453.

Ormières, D. & Provansal, M. 1999 Transition to turbulence in the wake of a sphere. *Phys. Rev. Lett.* **83**, 80–83.

Patera, A. 1984 A spectral element method for fluid dynamics: laminar flow in a channel expansion. *J. Comput. Phys.* **54** (3), 468–488.

Strogatz, S. H. 1994 *Nonlinear Dynamics and Chaos*. Addison-Wesley.

Tang, L. & Johnson, A. T. 1990 Flow visualization of mixed convection about a sphere. *Intl Comm. Heat Mass Transfer* **17**, 67–77.

Thompson, M., Hourigan, K. & Sheridan, J. 1996 Three-dimensional instabilities in the wake of a circular cylinder. *Exp. Therm. Fluid Sci.* **12**, 190–196.

Wang, A.-B., Trávníček, Z. & Chia, K.-C. 2000 On the relationship of effective Reynolds number and Strouhal number for the laminar vortex shedding of a heated circular cylinder. *Phys. Fluids* **12**, 1401–1410.

Wong, K. L., Lee, S. C. & Chen, C. K. 1986 Finite element solution of laminar combined convection from a sphere. *J. Heat Transfer* **108**, 860–865.

Wu, M.-H. & Wang, A.-B. 2007 On the transitional wake behind a heated circular cylinder. *Phys. Fluids* **19**, 084102–1–9.

Wu, S. J., Miau, J. J., Hu, C. C. & Chou, J. H. 2005 On low-frequency modulations and three-dimensionality in vortex shedding behind an normal plate. *J. Fluid Mech.* **526**, 117–146.

Yuge, T. 1960 Experiments on heat transfer from spheres including combined natural and forced convection. *J. Heat Transfer* **82**, 214–220.